ISSN 8755-6839

SCIENCE OF **TSUNAMI HAZARDS**

Journal of Tsunami Society International

Volume 34 **Number 3** **2015**

ON THE FREQUENCY SPECTRUM OF TSUNAMI RADIATION 144

Frank C Lin, Kingkarn Sookhanaphibarn, Worawat Choensawat - *Multimedia Intelligent Technology Laboratory, School of Science and Technology, Bangkok University, Bangkok,* ***THAILAND***
George Pararas-Carayannis - *Tsunami Society International, Honolulu, Hawaii,* ***USA***

NUMERICAL SIMULATION OF UJONG SEUDEUN LAND SEPARATION CAUSED BY THE 2004 INDIAN OCEAN TSUNAMI, ACEH-INDONESIA 159

Musa Al'ala[1, 3], Syamsidik[3, 4], Teuku Muhammad Rasyif[2, 3], and Mirza Fahmi[2,]
[1] *Student at Civil Engineering Department, Syiah Kuala University, Jl. Syeh Abd, Banda Aceh,* ***INDONESIA.*** musaalala@gmail.com
[2] *Post graduate student at Civil Engineering Master Program, Syiah Kuala University, Banda Aceh,* ***INDONESIA****.*
[3] *Tsunami and Disaster Mitigation Research Center, Syiah Kuala University, Jl. Prof. Ibrahim Hasan, Gampong Pie, Banda Aceh,* ***INDONESIA****.*
[4] *Civil Engineering Department, Syiah Kuala University, Banda Aceh, 23111,* ***INDONESIA.***

COASTAL RISK IN THE ALGIERS REGION (ALGERIA): INSIGHTS FROM TSUNAMI VELOCITIES, SEISMIC GROUND MOTION AND REMOTE SENSING 173

L. A. Amir, A. Dahlab, M.B. Douaifia
USTHB-FSTGAT, Department of Geophysics, BP 32, 16111 Bab Ezzouar, Algiers, ***ALGERIA***

B. Theilen-Willige - *Institute of Applied Geosciences, Berlin University of Technology (TU Berlin), Berlin,* ***GERMANY***

VALIDATION OF JOKO TINGKIR SOFTWARE USING TSUNAMI IMPORTANCE 189

Madlazim[1], Tjipto Prastowo[1] and Thomas Hardy[2]
[1]*Physics Department, State University of Surabaya (Unesa), Surabaya,* ***INDONESIA****,*
email: ***madlazim@fmipa.unesa.ac.id***
[2]*Indonesian Agency for Geophysics, Climatology and Meteorology, Jakarta 10720,* ***INDONESIA***

WWW.TSUNAMISOCIETY.ORG

TSUNAMI SOCIETY INTERNATIONAL, 1741 Ala Moana Blvd. #70, Honolulu, HI 96815, USA.

SCIENCE OF TSUNAMI HAZARDS is a CERTIFIED OPEN ACCESS Journal included in the prestigious international academic journal database DOAJ, maintained by the University of Lund in Sweden with the support of the European Union. SCIENCE OF TSUNAMI HAZARDS is also preserved, archived and disseminated by the National Library, The Hague, NETHERLANDS, the Library of Congress, Washington D.C., USA, the Electronic Library of Los Alamos, National Laboratory, New Mexico, USA, the EBSCO Publishing databases and ELSEVIER Publishing in Amsterdam. The vast dissemination gives the journal additional global exposure and readership in 90% of the academic institutions worldwide, including nation-wide access to databases in more than 70 countries.

OBJECTIVE: Tsunami Society International publishes this interdisciplinary journal to increase and disseminate knowledge about tsunamis and their hazards.

DISCLAIMER: Although the articles in SCIENCE OF TSUNAMI HAZARDS have been technically reviewed by peers, Tsunami Society International is not responsible for the veracity of any statement, opinion or consequences.

Submit manuscripts of research papers, notes or letters to the Editor. If a research paper is accepted for publication the author(s) must submit a scan-ready manuscript, a Doc, TeX or a PDF file in the journal format. Issues of the journal are published electronically in PDF format. There is a minimal publication fee for authors who are members of Tsunami Society International for three years and slightly higher for non-members. Tsunami Society International members are notified by e-mail when a new issue is available. Permission to use figures, tables and brief excerpts from this journal in scientific and educational works is granted provided that the source is acknowledged.

Recent and all past journal issues are available at: http://www.TsunamiSociety.org CD-ROMs of past volumes may be purchased by contacting Tsunami Society International at postmaster@tsunamisociety.org Issues of the journal from 1982 thru 2005 are also available in PDF format at the U.S. Los Alamos National Laboratory Library http://epubs.lanl.gov/tsunami/

ISSN 8755-6839

SCIENCE OF **TSUNAMI HAZARDS**

Journal of Tsunami Society International

Volume 34 **Number 3** **2015**

ON THE FREQUENCY SPECTRUM OF TSUNAMI RADIATION

Frank C Lin[1,*], Kingkarn Sookhanaphibarn[1], Worawat Choensawat[1], George Pararas-Carayannis[2]

[1]Multimedia Intelligent Technology Laboratory, School of Science and Technology, Bangkok University, Rama 4 Rd, Khlong Toei, Bangkok 10110, Thailand

[2]Tsunami Society International, Honolulu, Hawaii 96815, USA

ABSTRACT

We have measured the spectrum of the tsunami radiation at the following wavelengths: 0.73 μm, 10.8μm, 12.0μm, 6.8μm and 3.8 μm (or 13,698 cm^{-1}, 925 cm^{-1}, 833 cm^{-1}, 1,470 cm^{-1} and 2,631 cm^{-1} in wave numbers). By comparing with infrared spectroscopic measurements of water, we are able to identify these transitions corroborating our hypothesis that the radiation originates from the transition of vibrational quantum energy levels of water molecules in aggregate. We have also repeated our previous study of the decay rate of tsunamis for a different tsunami. An estimate of the intensity of the tsunami radiation is made.

Keywords: *remote sensing, quantum mechanics, tsunami radiation, frequency spectrum, infrared spectroscopy, tsunami decay*

Vol. 34, No. 3, page 144 (2015)

**Corresponding author. Email: linbfrank@gmail.com. Tel/Fax: +662 612 4705*

1. INTRODUCTION

In previous studies [Lin *et al*, 2010; Lin and Sookhanaphibarn, 2011; Lin *et al.*, 2011; Lin *et al.*, 2012; Lin *et al.*, 2013; Lin *et al.*, 2014] we have reported our observation that a tsunami emits radiation at 11 μm which can be observed by a geostationary satellite in the infrared domain. In the present study we investigate the origin of this radiation by considering the molecular properties of water in its excited quantum states. Also in previous studies [Lin *et al.*, 2013; Lin *et al.*, 2014] we have experimentally determined the decay rate of a tsunami by exhibiting the time series of the tsunami signal (the pixel brightness) in hourly intervals. Here we shall extend our previous work by considering a different tsunami and measuring half hour intervals. Our result confirms our previous work. We also posit that the 0.73μm emission near the borderline of the spectral sensitivity of the human eye may present a spectacular show of nature.

2. QUANTUM PROPERTIES OF WATER

The water molecules in the ocean are nonlinear, triatomic molecules with the shape of an asymmetric top. There are three unequal moments of inertia about three mutually perpendicular principal axis. They are capable of executing both rotational and vibrational motion. There are three rotational modes and three vibrational modes. Rotational levels of water are labeled by the quantum numbers ($J\ K_a\ K_c$), where J is the quantum number for the total angular momentum. The indices K_a and K_c refer to the angular momentum quantum numbers in the corresponding prolate and oblate symmetric tops. In an environment with tetrahedral symmetry or higher, each ($J\ K_a\ K_c$) level is $2J+1$ fold degenerate, with an additional quantum number M_J which is the angular momentum projection on the axis *a* and *c*. The rotational states are correlated to the proton spin states through the Pauli principle: ortho-water states have total nuclear spin $I = 1$, and odd parity for $K_a + K_c$ in the ground vibrational state. The para-water states have total nuclear spin $I = 0$, and even parity for $K_a + K_c$ in the ground vibrational state [Beduz et al., 2012]. Photons are emitted when the molecules execute a transition from a higher vibrational quantum level to a lower level. These photons are mostly in the terahertz frequency range. For water, these spectra have been measured experimentally by several spectroscopic laboratories [Coudert *et al*., 2004; Coudert, 1994; Coudert, 1997; Languetin et al., 1999; Languetin et al., 2001; Toth, 1991; Toth, 1993]. These experimental spectroscopic measurements have been corroborated by theoretical calculations obtained by solving the Schrödinger equation with the appropriate Hamiltonian. Recently the range of vibrational and rotational energy levels has been greatly extended using variational calculations [Tennyson *et al*., 2001]. It should be noted that these levels may be subject to experimental errors. In the case of tsunamis, *the water molecules are in rapid motion and frequently collide violently with each other*. This circumstance may cause a shift in the quantum energy levels due to the centrifugal and Coriolius forces.

Tsunamis are perhaps one of the most destructive natural events on earth, comparable to volcanic eruptions or a meteorite striking the earth. In order to obtain an intuitive understanding of the scale of a tsunami event, we make an order of magnitude estimate of quantities of water, molecules, radiation and power released by such an event. At the onset of the tsunami event, a great mass of

water is transferred from the bottom of the ocean to the surface. The horizontal dimension of this great mass of water is circa 10 km x 10 km (2 pixels by 2 pixels). Following the estimate of Levin et al [Levin *et al*., 1998], we shall assume that the thickness of the water layer affected by the upward pulse to be 1.5 km. The total volume of water is therefore 1.5×10^{11} m^3. This amounts to a total number of molecules given by the astronomical number of 4×10^{36}.

The total power P radiated for a transition from k to i in a spectral line of frequency ν is

$$P_{line} = (4\pi)^{-1} h\nu \, A_{ki} \, N_k \tag{1}$$

where A_{ki} is the transition probability and
N_k is the number of exited atoms in level k.

Numerically A_{ki} is related to the line strength Z as follows [Martin and Wiese, 1996]

$$A_{ki} = \frac{2{,}026.1 \times 10^8}{\lambda^3 g_k} \times Z \approx 1 \times 10^8 \, Z \tag{2}$$

where

$$g_k = \sum_k (2J_k + 1) \tag{3}$$

is the statistical weight and λ the wavelength. If we substitute typical order of magnitude values for the quantities $h \approx 10^{-34}$, $\nu \approx 10^{12}$, $A_{ki} \approx 10^8$, $N_k \approx 10^{36}$ and $Z \approx 1$ into Eq. (1), we obtain for the total power $P_{line} \approx 10^{21}$ radiated per unit solid angle [Martin and Wiese, 1996; Tennyson *et al*., 2001].

Equation (1) is dominated by the number of molecules making the transition, which ultimately determines the intensity of the radiation that we were able to detect by the geostationary satellite. Although quantum transitions are microscopic events characterized by the Planck constant h, the immensity of the tsunami as characterized by the number of molecules involved, N_k, transforms it to a real world macroscopic phenomenon.

3. THE SATELLITE

The satellite that we utilized is the Japanese meteorological satellite MTSAT-2. This satellite is stationed at an altitude of approximately 36,000 km above the equator in a geostationary orbit at longitude 145˚ E. It is a 3-axis altitude controlled geostationary satellite with an advanced Himawari

Imager. There are five data channels at five different frequencies. These channels are capable of making multi-purpose imagery and wind derivation by tracking clouds and water vapor features. The resolution is from 0.5 to 2 km depending on the wavelength. The wavelength covers a range from 0.47 to 13.3 μm. The coverage is a full disk for every 10 minutes. The satellite carries a transponder to relay environmental data from the data collection platform. Data transmission rate is 18 GHz.

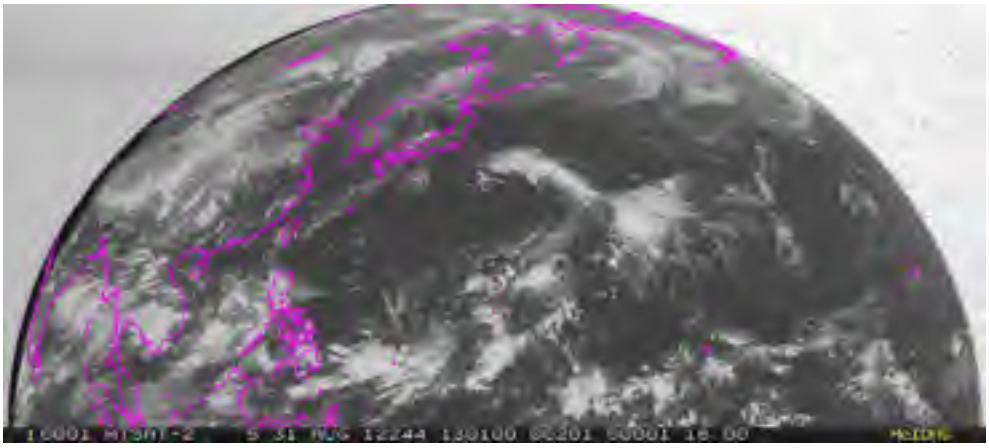

Fig. 1:MTSAT-2 satellite image on 2012-8-31 at 13:01 UTC at 3.75 microns

Under normal operations, the functions of the detectors are to record sea surface temperature, integrated water vapor, cloud cover, cloud top temperature etc. In our case we have shown [Lin *et al*, 2010; Lin and Sookhanaphibarn, 2011; Lin *et al.*, 2011; Lin *et al.*, 2012; Lin *et al.*, 2013; Lin *et al.*, 2014] that these detectors have also captured the tsunami radiation.

4. COMPARISON OF REMOTE SENSING AND SPECTROSCOPIC RESULTS

A seaquake of magnitude 7.6 on the Richter scale, positioned at latitude 10.8˚N and longitude 106.8˚E east of Soulangan, Philippines, took place at 12:48 UTC on 2012-08-31. In Table I we summarize the results obtained by examining satellite images from the MTSAT-2 taken on 2012-8-31 at 13:01 UTC. Images at the wavelengths 0.73 μm, 10.8 μm, 12.0 μm, 6.8 μm and 3.8 μm are recorded by the detectors of the satellite. In columns 1 and 2 of Table I we list the band and upper level quantum numbers from which the quantum transition took place. All transitions are to the ground level (0 0 0). The spectroscopic measurements reported by different authors are listed in column 5, which are compared with the frequencies detected by the satellite in column 4. We observe that they are overall compatible. The differences may be accounted for by the experimental errors of the satellite detectors and of the spectroscopic measurements, and by the shift in the spectral lines due to centrifugal and Coriolius forces. In addition, random translational motions of individual molecules leads to Doppler shift of absorption and emission wavelengths. We have only considered transitions to the ground state, although cascade transitions to higher levels (i.e. not to the ground state) are possible, and may have also been detected by the satellite [Toth, 1991; Toth, 1993; Lanquetin, 1999; Lanquetin, 2001]. The tsunami signal S is defined as the magnitude in pixels of the infrared radiation emitted by

the tsunami and measured directly from the satellite image [Lin *et al*, 2010; Lin and Sookhanaphibarn, 2011; Lin *et al.*, 2011; Lin *et al.*, 2012; Lin *et al.*, 2013; Lin *et al.*, 2014]. When referring to the satellite image, it is sometimes called the pixel brightness. A plot of the wavelength in microns versus the sine of the tsunami signal in pixels is shown in Fig.2.

Table 1: Spectroscopic & Satellite spectrum of H_2O at Soulangan at 13:01 UTC

Band	Upper Level $J\ K_a\ K_c$	λ μm	Satellite cm^{-1}	Spectroscopy cm^{-1}	S pixels	Reference
(030)	18 18 0	0.73	13,698	13,647	92	Coudert(2004)
(000)	7 4 4	10.8	925	927	258	Toth(1991)
(000)	7 3 4	12.0	833	842	173	Toth(1998)
(000)	9 5 5	6.8	1,470	1,474	209	Toth(1991)
(000)	13 5 8	3.8	2,631	2,629	119	Toth(1991)

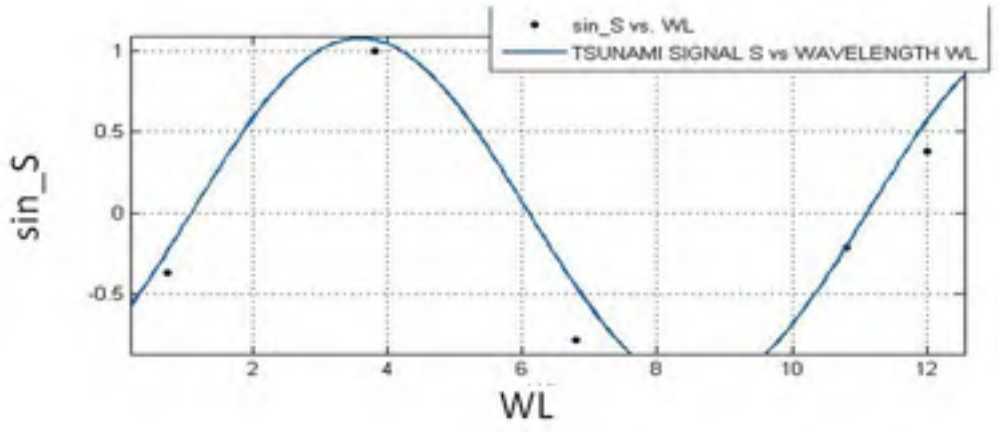

Fig.2: Sinusoidal behavior of tsunami signal vs. wavelength

The equation of interpolation is given below:

$$S = 1.076 * \sin(0.6256 * \lambda - 0.6703) \quad (4)$$

The parameters for the goodness of fit are: SSE: 0.1618, R-square: 0.916, and RMSE: 0.2844. This is solely an empirical relationship which suggests that the strength of the tsunami signal is not randomly distributed, (in which case we would obtain a scatter gram). We can interpret this relationship visually by considering Fig.3 in polar coordinates. If we equate the angle θ with the wavelength for the radiation detected by the satellite, λ, and the function f with the tsunami signal S, then we can conclude that the tsunami signal traces out the equipotential lines of a dipole for constant φ in the wavelength space (Fig.3). This diagram provides a graphical method for the calculation of the tsunami signal.

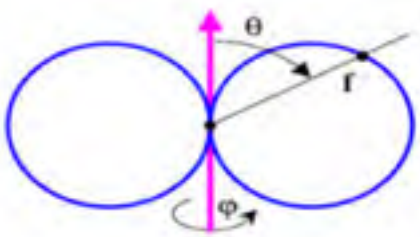

$$f\theta,\phi=A\cdot\sin^{10}(\theta)$$

Fig. 3: Geometrical interpretation for tsunami signal S

5. Time Series and Decay of Tsunamis

On 2012-08-31 at 12:47:34 UTC a seaquake with moment magnitude of 7.6 with epicenter at latitude 10.8˚N and longitude 106.8˚E occurred 96 km. east of Soulangan, Philippines. According to the USGS, this seaquake was an intraplate event, which resulted from reverse faulting within the oceanic lithosphere in the region between the Philippines Sea plate and the Sunda plate. Tectonically, the Philippine Sea plate is bounded by the larger Pacific and Eurasian plates and the smaller Sunda plate. At the latitude of the seaquake, the Philippines Sea plate moves west northwestward at a velocity of approximately 10 cm/year with respect to the Sunda plate [Pararas-Carayannis, 2013]. The following figure show the MTSAT-2 infrared satellite image of the Philippines on 2012-08-31 at 10.8 μm at 13.01 UTC: This image is made just 13 min after the seaquake took place.

From this satellite image we make a cross-sectional cut from north to south along the longitude 106.8˚E and obtain the North-South signal diagram. The procedure to accomplish this is described in reference [Lin *et al.*, 2010; Lin *et al.*, 2014]:

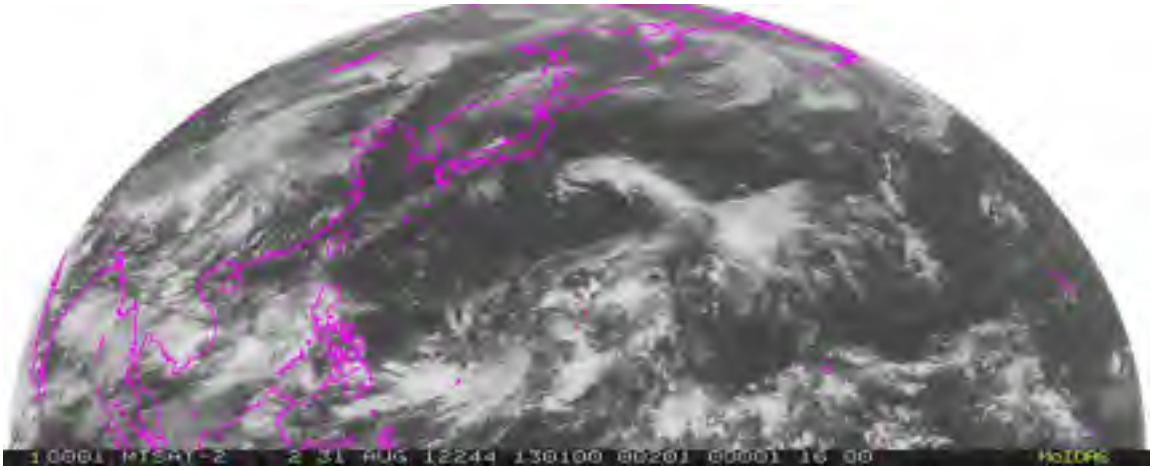

Fig. 4: Satellite image of Soulangan on 2012-08-31 at 13:01 UTC and wavelength 10.8 µm

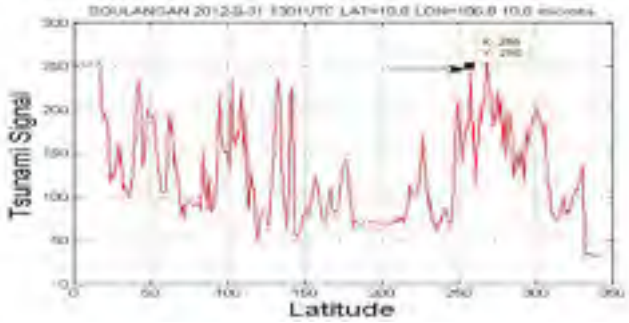

Fig.5: North-South signal diagram for Soulangan on 2012-8-31 at 13.01 UTC for 10.8µm

An arrow points to the tsunami signal at latitude 10.8˚ or 258 pixels. A similar diagram can be constructed for a cut along the East-West axis (i.e. along 10.8˚E latitude, which we call the East-West signal diagram).

In order to construct a Time Series to investigate the rate of decay of the tsunami signal, we have measured the signal at 13:01, 13:32, 14:01, 15:01 and 16:01 UTC, and for the five available frequencies 0.73, 3.8, 6.8, 10.8 and 12.0 µm. The result is summarized in Table 2 in Appendix A. In the following we discuss the decay pattern of each of these channels.

A. The IR-4 channel:

At 10.8 μm, this is the long wave length or IR-C (also classified as IR-4) band, which is the band utilized in our previous investigations [Lin *et al*, 2010; Lin and Sookhanaphibarn, 2011; Lin *et al.*, 2011; Lin *et al.*, 2012; Lin *et al.*, 2013; Lin *et al.*, 2014]. The IR photon energy is between 0.001 and 1.7 eV. This is the atmospheric window covered by detectors such as HgCdTe and microbolometers. Satellite images in this frequency region can be used to determine cloud heights and types, to calculate land and surface water temperatures, and to locate ocean surface features. These infrared pictures are also used to depict ocean eddies or vortices and map currents. And, as we have demonstrated in our previous work, it can be used to detect tsunami signals. Fig. 6 shows the Time Series for Tsunami Signal for 10.8 μm.

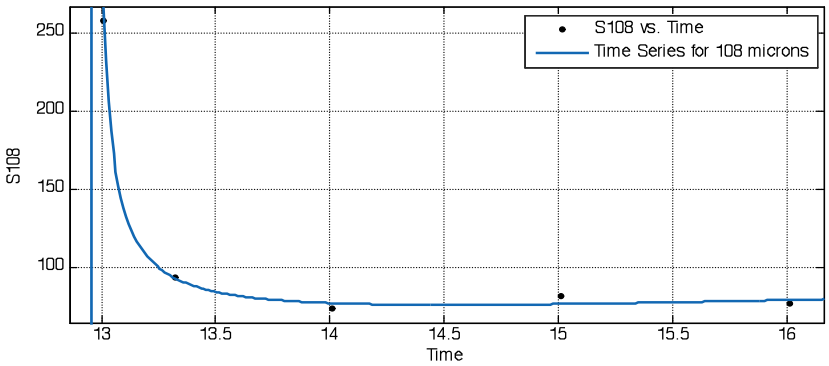

Fig. 6: Time series for tsunami signal for 10.8 μm

We observe that the signal has decayed by approximately ¾ after half an hour's time has lapsed and remained at that level. There is no rebound within a period of three hours, indicating that the tsunami effect has dissipated.

B. The IR-5 Channel:

The following figure, Fig.7, shows the Time Series for 12.0 μm, which is also in the IR-C band (IR-5). The behavior is similar to the previous case, although there is a steady rise of the tsunami signal with time. Since we do not observe this behavior with the other channels, it is likely that it is not directly associated with the tsunami.

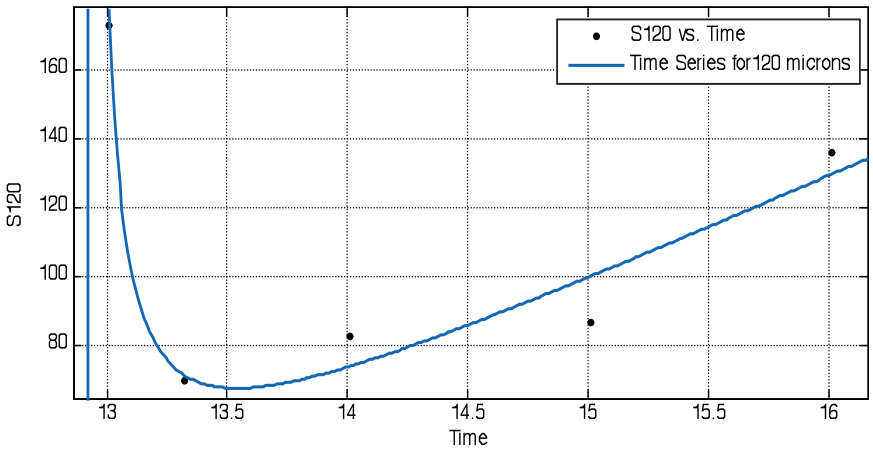

Fig. 7: Time series for tsunami at 12.00 µm.

C. The Water Vapor channel at 6.75 µm:

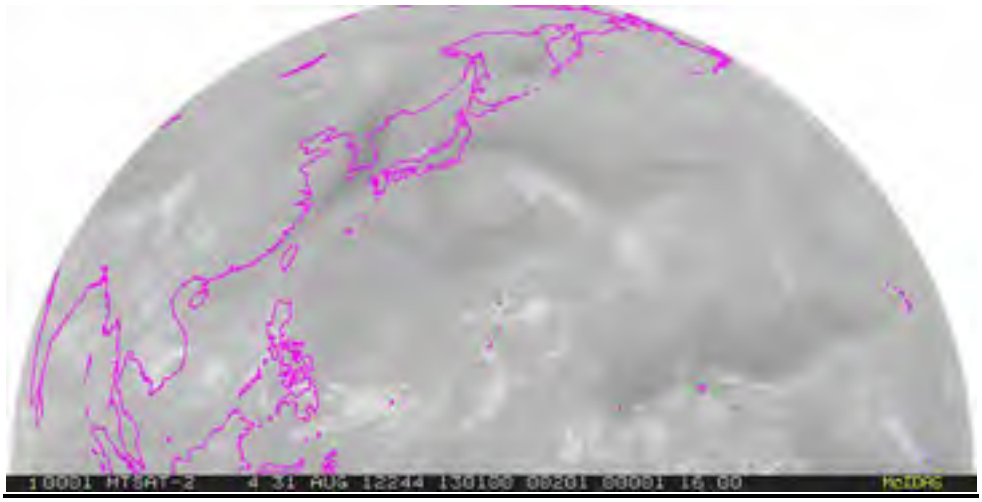

Fig. 8: MTSAT-2 satellite image of Soulangan at 13:01 UTC at 6.75 µm

The water vapor channel (from 6.40 to 7.08 µm) shows the amount of moisture in the atmosphere. This channel is the most important IR absorber. Fig. 9 shows the time series at 6.75 µm. We note that the band around 6.3 µm (1590 cm^{-1}) is due to the H-O-H bending vibration.

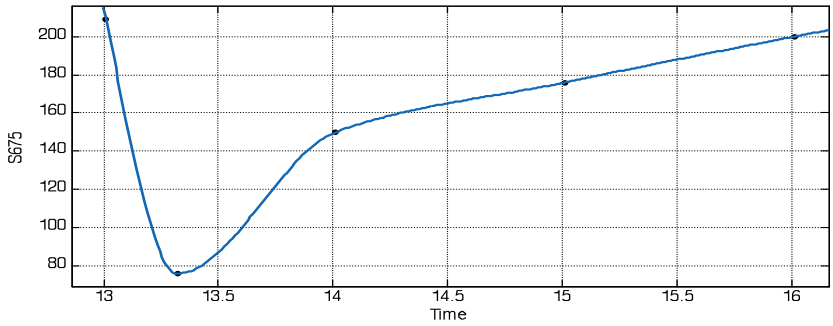

Fig. 9: Time series of tsunami for water vapor channel

We observe that the tsunami signal starts to rise half an hour after the onset of the tsunami and continues this trend, albeit at a slow rate of change. This behavior suggests that immediately after the decay the moisture content of the atmosphere begins to unravel due to local atmospheric variations possibly due to wind and that the tail of the Time Series is not directly related to the tsunami *per se*. This implies that the water vapor channel is a poor choice for the observation of the tsunami signal.

D. The Intermediate Infrared Channel:

The intermediate infrared channel (IIR) at 3.75 μm also belongs to the IR-C band in the infrared spectrum. This band is used for tracking, for example, by heat seeking missiles. The Time Series, as shown in Fig.10, shows the typical behavior of tsunami decay. The decay occurs within half an hour, and then maintains a constant nadir. This channel is therefore suitable for investigating tsunami onsets.

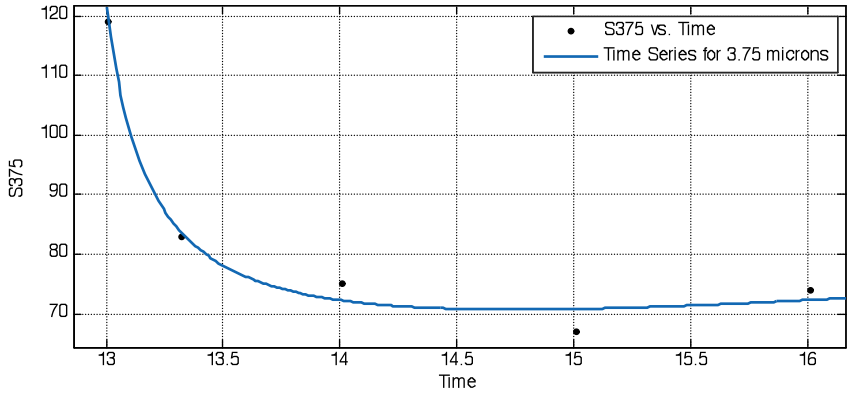

Fig.10 Time series for the 3.75 μm channel

E. The Near Infrared Band:

This relatively higher frequency channel is in the Near Infrared (IR-A) spectra range which is characterized by water absorption, and commonly used in fiber optic telecommunication because of low attenuation losses in the SiO_2 glass. It is at the borderline of detection by the human eye since it is closest to the visible spectrum.

However, since the transition took place from a relatively high level, (0 3 0), to the ground state, the transition probability will be weaker and the intensity of radiation will be reduced (see Table I). The Schrödinger wavefunction ψ for the water molecule in this excited state is given by a linear combination of the symmetric O-H stretch, v_1, and the antisymmetric stretch v_3: $\psi = av_1 + bv_3$, where a and b are constants. The bending contribution v_2 is not present. We speculate that the tsunami onset may be observable by a passenger in a ship inadvertently navigating in the vicinity. If visible at all, he would perceive the event as a burst of dull, deep red afterglow, extending approximately for 10 km in every direction, and disappearing within half an hour. It could be one of the most spectacular displays of nature. This is therefore another suitable channel for the investigation of tsunamis.

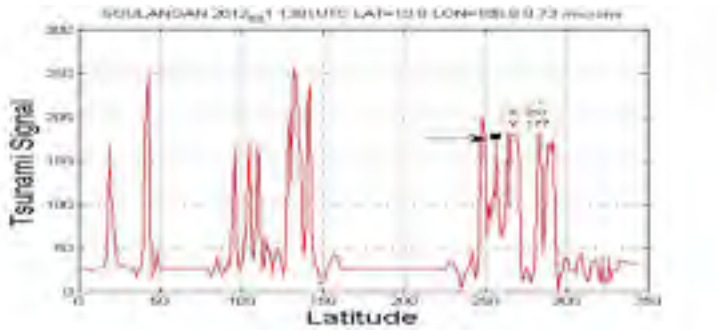

Fig. 11: North-South signal diagram for Soulangan at 13:01 UTC on 2012-8-31 at 0.73 microns

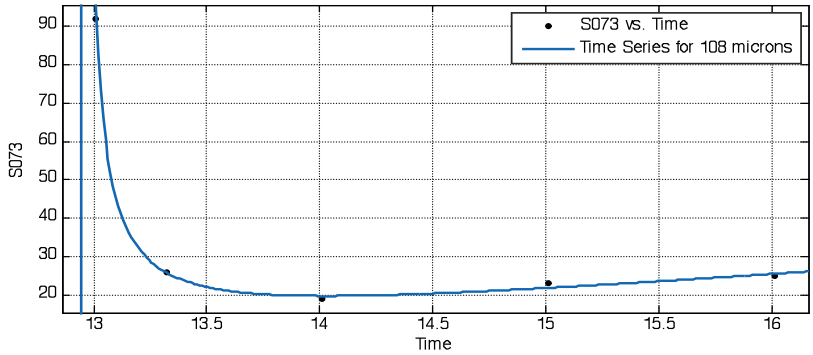

Fig.12: Time series for the 0.73 μm channel

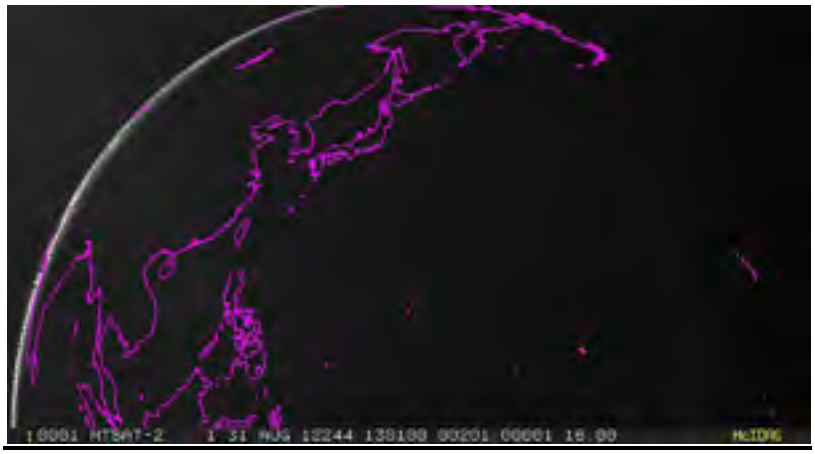

Fig. 13: MTSAT-2 satellite image of Soulangan 2012/8/31 13:01 UTC at 0.73 microns

In the above, Fig.11 shows the North-South signal diagram, Fig. 12 the time series, and Fig.13 the MSAT-2 satellite image for this channel.

6. Conclusion

We conclude as follows:

1) We have demonstrated experimentally that the tsunami radiates at all frequencies in the infrared range and decays within half an hour. We suggest that the eye of the tsunami may be visible to the naked human eye since it emits radiation at 0.73 μm which is at the borderline of spectral sensitivity.

2) We have shown that the infrared radiation detected by the geostationary satellite can be accounted for by transitions between vibrational quantum levels of water molecules. We cannot exclude, however, the possibility that another source of radiation may also be present. Novik *et al.* [2014] have shown that, on the basis of a 3D model, a moving oceanic lithosphere can generate electromagnetic disturbances and after propagation to the earth surface emit radiation into the atmosphere. However, the frequency interval predicted by this mechanism is not in the infrared range. Some impurities in the ocean, such as sand (SiO_2), are capable of emitting infrared radiation but they are quantitatively insignificant. Among the quake precursor events is often a special cloud formation above the stress area of a potential fracture of a fault. It appears that precursory stresses (perhaps of electromagnetic nature and resulting friction and Coulomb stress), among other precursor events (radon, hydrogen emissions, etc), break down the water of hydration in the hard rocks, or perhaps affect the water molecules of the sea by breaking their hydrogen bonding that holds them together. Love and Raleigh seismic surface waves may play a role on altering the quantum state of the sea water molecules, thus

resulting in the release of photons or other infrared radiation. We are not aware of interference by other molecules in the atmosphere (CO_2, N_2, water droplets etc) at these frequencies. It is likely that the tsunami broadcasts infrared radiation at many different frequencies corresponding to transitions from many different rotational-vibrational quantum energy levels, and that we have only, *par hasard*, measured five of these by our satellite. In view of the richness of the molecular spectra of water, it is not unjustified to hypothesize that the tsunami is playing a symphony with many chords.

7. APPENDIX A

Table 2: Time series & frequency dependence of tsunami radiation

Location	**Sat**	**Lat N**	**Lon E**	**Date**	**Image Time**	λ μm	M_e	S^1 pixels	**REM**
Soulangan	MTSAT2	10.8	106.8	2012_8_31	13:01	3.75	7.6	119	Low cloud
Seaquake at 12:48UTC						12.0		173	Cloud temp
						10.8		258	Cloud top
						0.73		92	Surface feature
						6.75		209	WV
	MTSAT2				13:32	3.8		83	
						12.0		70	
						10.8		94	
						0.73		26	
						6.8		76	
	FY2E				14:01	3.8		None*	
						12.0		83	
						10.8		74	
						0.73		19	
						6.8		150	
	MTSAT2				15:01	6.8		176	
						12.0		87	
						3.8		67	
						10.8		82	
						0.73		23	
	MTSAT2				16:01	6.8		200	
						12.0		136	
						3.8		74	
						10.8		77	
						0.73		25	

*Cancelled due to eclipse. An average value is used. [1]measured by East West Signal

REFERENCES

Beduz, C, M.Carravetta, J. Y. C. Chen, M. Concistre, M. Denning, M. Frunzi, A. J. Horsewill, O. G. Johannessen, R. Lawler, X. Lei, M. H. Levitt, Y. Li, S. Mamone, Y. Murata, U. Nagel, T. Nishida, J. Ollivier, S. Rols, T. Rööm, R. Sarkar, N. J. Turro, Y. Yang, 2012. Quantum rotation of *ortho* and *para*-water encapsulated in a fullerene cage: Proceedings of the National Academy of Science 109, pp. 12894-12898.

Coudert, L.H., 1994. Analysis of the Rotational Levels of Water and Determination of the Potential Energy Function for the Bending ν_2 Mode: J. of Mol. Spectroscopy 165, pp.406-425.

Coudert, L.H., 1997. Analysis of the Line Positions and Line Intensities in the ν_2 Band of the Water Molecule: J. of Mol. Spectroscopy 181, pp.246-273

Coudert, L.H., O.Pirali, M.Vervloet, R.Languetin and C.Camy-Peyret, 2004. The eight first vibrational states of the water molecule: measurement and analysis. J. of Molecular Spectroscopy 228, pp. 471-498.

Lanquetin, R., L.H.Coudert and C.Camy-Peyret, 1999. High-Lying Rotational Levels of Water: Comparison of Calculated and Experimental Energy Levels for (0 0 0) and (0 1 0) up to J=25 and 21. J. of Mol. Spectroscopy 195, 54-67.

Lanquetin, R., L.H.Coudert and C.Camy-Peyret, 2001. High-Lying Rotational Levels of Water: An Analysis of the Energy Levels of the Five Vibrational States: J. of Mol. Spectroscopy 206, 83-103.

Levin B.V., M.A.Nosov, V.P.Pavlov and L.N.Rykunov, 1998. Cooling of the Ocean Surface as a Result of Seaquakes. Doklady Earth Sciences Vol.358, No.1, pp. 132-135.

Lin F.C., K. Na Nakornphanom, K. Sookhanaphibarn, and C. Lursinsap, 2010. "A New Paradigm for Detecting Tsunamis by Remote Sensing"; International Journal of Geoinformatics, Vol.6, No.1, March 2010, pp.19-30.

Lin F.C. and K. Sookhanaphibarn, 2011. Representation of Tsunamis in Generalized Hyperspace: Proceedings of the IEEE International Geoscience and Remote Sensing Symposium (IGARSS'11), Sendai/Vancouver, July 21, 2011. pp. 4355-4358.

Lin F.C., W. Zhu and K. Sookhanaphibarn, 2011. Observation of Tsunami Radiation at Tohoku by Remote Sensing, Science of Tsunami Hazards, Vol.30, No.4,Honolulu, HI, December 2011, pp. 223-232.

Lin, F.C., W. Zhu and K. Sookhanaphibarn, 2012. A Detail Analysis of the Tohoku Tsunami by Remote Sensing, Proceedings of the IEEE International Geoscience and Remote Sensing Symposium (IGARSS'12), Munich, Germany, pp.1166-1169.

Lin. F.C., W. Zhu, K. Sookhanaphibarn and P. Silapasuphakornwong, 2013. REMOTE:-A Satellite Based Tsunami Early Warning Detection System, Proceedings of the IEEE International Geoscience and Remote Sensing Symposium (IGARSS' 13), Melbourne, Australia, pp. 3694-3697.

Lin, F.C., K. Sookhanaphibarn, V. Sa-yakanit and G. Pararas-Carayannis, 2014. REMOTE: Reconnaissance & Monitoring of Tsunami Events, Science of Tsunami Hazards, Vol.33, No.2, pp.86-111

Martin, W.C. and W.L.Wiese, 1996. Atomic, Molecular and Optical Physics Handbook, G.W.R.Drake, Ed., AIP Press, Woodbury, N.Y.

Novik, O., S. Ershov, Y. Ruzhin, F. Smirnov and M. Volgin, 2014. Theory and detection scheme of seismic EM signals transferred into the atmosphere from the oceanic and continental lithosphere. Advances in Space Research 54, pp. 168-184.

Pararas-Carayannis, G., 2013. "The Great Tohoku-Oki Earthquake and Tsunami of March 11, 2011 in Japan: A Critical Review and Evaluation of the Tsunami Source Mechanism," Pure and Applied Geophysics, pp. 1-22.

Tennyson, J., N.F. Zobov, R. Williamson, O.L. Polyansky, P.F. Bernath, 2001. Experimental energy levels of the water molecule. Journal of Physical and Chemical Reference Data, 30 (3). pp. 735-831.

Toth, R. A., 1991. ν_2 band of $H_2{}^{16}O$: line strengths and transition frequencies. J. Opt. Soc. Am. B, Vol.8, No.11, November 1991, pp.2236-2255.

Toth, Robert A., 1993. $2\nu_2 - \nu_2$ and $2\nu_2$ bands of $H_2{}^{16}O$, $H_2{}^{17}O$ and $H_2{}^{18}O$: Line Positions and Strength: J. Opt. Soc. Am. B, Vol.10, No.9, September 1993, pp. 1526-1544.

ISSN 8755-6839

SCIENCE OF TSUNAMI HAZARDS

Journal of Tsunami Society International

Volume 34 Number 3 2015

NUMERICAL SIMULATION OF UJONG SEUDEUN LAND SEPARATION CAUSED BY THE 2004 INDIAN OCEAN TSUNAMI, ACEH-INDONESIA

Musa Al'ala[1, 3], Syamsidik[3, 4], Teuku Muhammad Rasyif[2, 3], and Mirza Fahmi[2,]

1 Student at Civil Engineering Department, Syiah Kuala University, Jl. Syeh Abd. Rauff, No.7, Banda Aceh, 23111 Indonesia.
2 Post graduate student at Civil Engineering Master Program, Syiah Kuala University, Jl. Syeh Abd. Rauff, No.7, Banda Aceh, 23111. Indonesia.
3 Tsunami and Disaster Mitigation Research Center, Syiah Kuala University, Jl. Prof. Ibrahim Hasan, Gampong Pie, Banda Aceh, 23233 Indonesia.
4 Civil Engineering Department, Syiah Kuala University, Jl. Syeh Abd. Rauff, No. 7, Banda Aceh, 23111, Indonesia.
musaalala@gmail.com

ABSTRACT

The Aceh province in Indonesia, located around the Sumatra subduction area, was one of the worst hit areas with respect to damage from the impact of the 2004 Indian Ocean tsunami. A 9.15 Mw earthquake triggered the tsunami. One of the impacts was the disconnection of several areas from their mainland, thus creating new small islands. This happened around Ujong Seudeun village in Aceh Jaya District. Prior to the tsunami, the village had approximately 500 residents. However, after the tsunami, the area was severely eroded and a small strait had been inserted between the village and the Sumatra Island mainland. This study investigates the magnitude of the tsunami wave forces that separated the area to yield a newly deserted small island. This study was conducted by numerical simulations and by coupling the COMCOT (Cornell Multi-grid Coupled Tsunami Model) and Delft3D models. These tools have specific advantages, namely, COMCOT's linear modeling is based on a series of earthquake mechanisms and Delft3D uses non-linear morphological dynamic modeling. Their software includes the explicit leapfrog finite difference scheme (COMCOT) and the non-linear shallow water equation (Delft3D). Bathymetry data from

newly formed coastline and the small island's shape were digitized using 2005 Quickbird Images. Results from this research reveal the estimated tsunami wave heights and forces that disconnected the small island of Ujong Seuden from the Sumatra Island mainland. These results can be used to further develop the COMCOT model to incorporate sediment modules.

Keywords: *morphology, erosion, and tsunami wave height, COMCOT, Delft3D.*

1. INTRODUCTION

The Aceh province in Indonesia, located around the Sumatra subduction area, was one of the worse areas with respect to damage from the impact of the 2004 Indian Ocean tsunami. A 9.15 Mw earthquake triggered the tsunami. One impact was the disconnection of several areas from their mainland to create small islands such as those around the village of Ujong Seudeun. This village is located in Aceh Jaya District near the Geurutee mountainside. Before the tsunami, this village had approximately 500 residents, but today, this village has no permanent residents. Locals now utilize this area solely for beef husbandry and coconut farming. Ujong Seudeun is now constrained by the massive sediment transport that caused the land separation. With respect to impact of tsunami waves on sediment transport, the tsunami deposit has generated a lot of research interest (Dawson et al. 1996; Moore et al. 2007; Shi et al. 1995; Gelfenbaum and Jaffe 2003; Richmond et al. 2012). Studies have focused on determining how the tsunami made its impact and how the hydrodynamic forces worked to separate the land bar. For time and efficiency considerations, numerical simulations are required to investigate these phenomena. The research based on numerical simulation with respect to combine tsunami propagation and sediment transport is rarely and it still needs some improvement. This paper is aimed at investigating the process of the land separation due to the tsunami wave forces by means of numerical simulations'. The tsunami waves propagation and sediment transport produced during the propagation can be analyzed with numerical modeling. The tsunami waves propagation can been conducted using COMCOT (Cornell Multi- grid Coupled Tsunami Model) (Liu et al., 1994; 1998). To simulation near shore process including sediment transport, Delft3D-FLOW developed by Deltares (2007) of the Netherland offers some advantages. In this study, tsunami propagation is simulated with COMCOT using the leap-frog finite difference based on a series of earthquake mechanisms. The COMCOT results are then used as input for a sediment transport simulation using Delft3D-FLOW and its non-linear shallow water equation. The result would appeal the process of the sediment transport coupled with Delft3D-FLOW in producing close fitted result from COMCOT tsunami propagation. This paper provides the first physical explanation ever on the creation of a new Island of Ujong Seudeun in Aceh after the 2004 Indian Ocean tsunami.

2. STUDY AREA

Ujong Seudeun is an area in Aceh Jaya, near the Geurutee mountainside. Located between 5.116847° N and 95.294216° E, Ujong Sedeun is 75.1 km from Banda Aceh, the capital city of the Aceh province. Prior to the tsunami, this area had approximately 500 residents and had an infrastructure, including a mosque and houses. Since the tsunami hit Aceh, following the 2004 megathrust earthquake, Ujong Seudeun has been deserted. Because the land connectin Ujong Seudeun with the main island was swept away, its residents were forced to move to the main island. A 1519-m-long area eroded after the tsunami, leaving Ujong Seudeun completly separated

from the island. The tsunami wave and natural interventions since that time have transformed 1,538,854 m^2 of land into ocean (according to shoreline comparations on Google Earth images taken on June 23, 2003 and March 2, 2011).

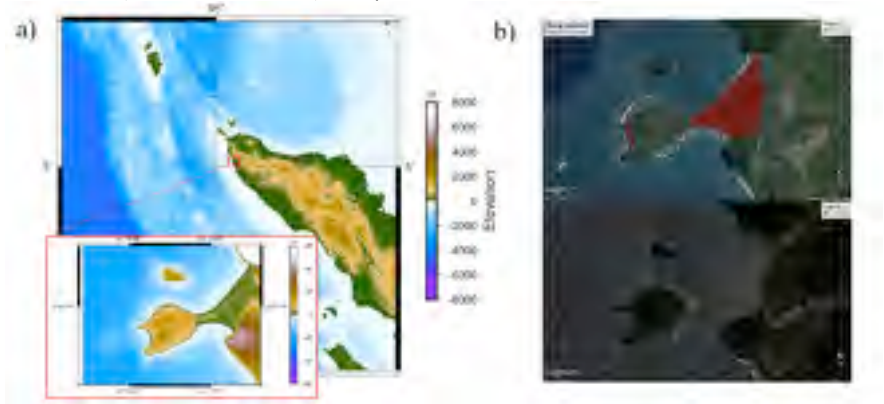

Figure 1. (a) Ujong Seudeun on Sumatra Island and (b) Ujong Seudeun area before and after the 2004 Indian Ocean Tsunami by Google Earth image.

3. METHOD

First, we began the numerical simulation process by preparing the data for layer setup. We used General Bathymetric Chart of the Oceans (GEBCO) data for the larger grid (layers 1 and 2), and for layers 3 and 4, we used GEBCO data with a smaller grid size and updated it with available navigation charts. We used a multi-fault machanism developed by Romano (2009) and employed these data to run a 3-hour COMCOT simulation. We then analyzed the hydrodynamic data produced by the COMCOT simulation to determine the shear stresses that had occurred. The simulation was then continued for the sediment transport process using Delft3D-FLOW as it also has been helpful for the tsunami propagation (Vatvani et al., 2012). In addition, we used the hydrodynamic data from the fourth layer elevation data as input for Delft3D-FLOW.

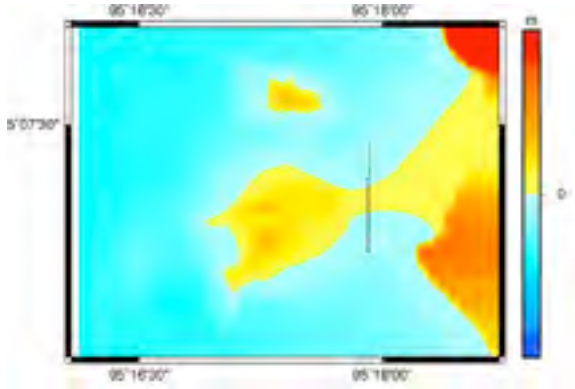

Figure 2. Layer 4 with 28 observation points.

Hydrodynamic forces affect the water depth and area characteristics. To investigate the operation of these forces, we applied data from 28 observation points located across the land bar area in the COMCOT simulation, as shown in Figure 2. Each observation point was 50 m long. In addition, we applied 4 other observation points at each edge of the water area in layer 4. These extra observation points provided water depth and depth-averaged velocity data for the Delft3D-FLOW input, as boundary data. Observation points were also applied in the Delft3D-FLOW simulation to record the sediment transport process that occurred.

3.1 Fault Model

The 2004 megathrust earthquake located at 95.8° E and 3.4° N resulted in significant dislocation. The earthquake occurred at 07:59 am local time and within 8 to 10 min caused ruptures to the western coast of northern Sumatra Island as far as 1200–1300 km from the Andaman–Sunda Sea. The complex fault mechanism of the rupture process is difficult to explain. To describe the complexity of the multi-fault mechanism, several researchers have proposed earthquake source parameters. In this research, we used the multi-fault mechanism developed by Romano (2009). This model was also used by Liu et al. (2012) to investigate the morphological changes in Aceh from the 2004 tsunami. As explained by Okada (1985), tsunamis are generated by the deformation of the sea floor, which is instantly reproduced at the sea surface. This theory is also known as the deformation model.

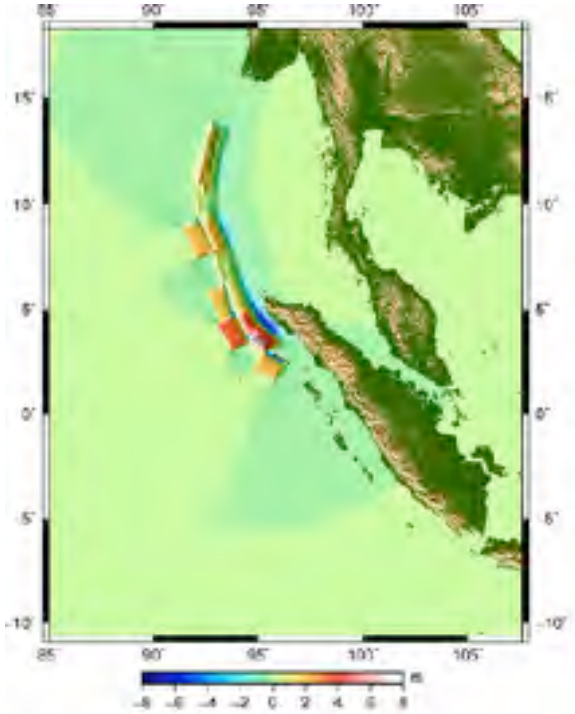

Figure 3. Initial condition and earthquake epicenter for 2004 tsunami.

3.2 Grid Set up

We performed the numerical simulation using an equation that could process a large amount of data. A dynamic coupled system of nested grids was employed to simulate the tsunami propagation from the Andaman–Sumatra subduction zone toward the location under consideration (Wang and Liu, 2008). COMCOT uses a nested grid system with 4 layers of different size and resolution and has its own shallow water equation (linear or non-linear). In the first layer, we used GEBCO data with a grid resolution of 1 min (1851 m), and the rupture area was located in the simulation area. Almost identical to the first layer, we also used GEBCO data in layer 2, interpolated into a 0.1667-min grid (308.5 m).

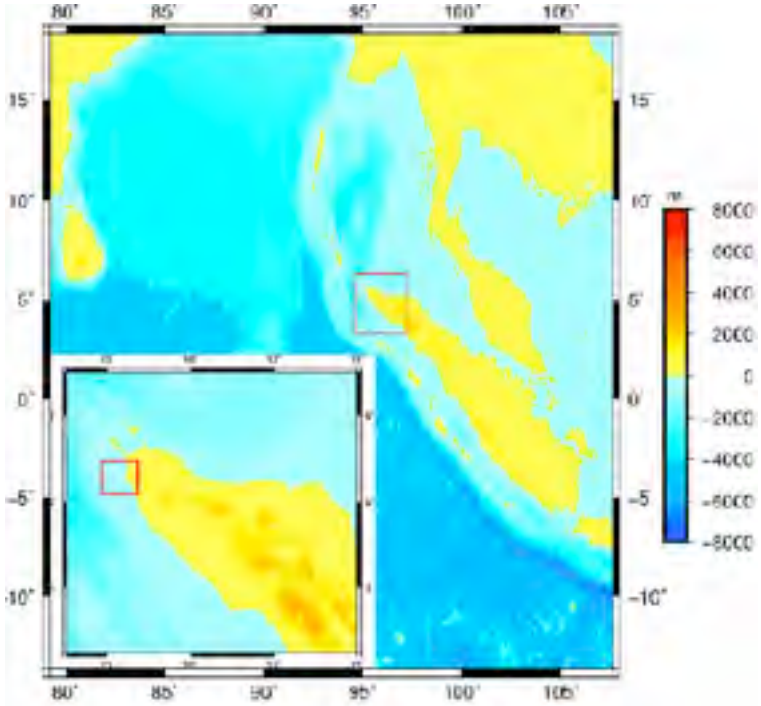

Figure 4. Layer 1 of computational domain with layer 2 marked in a red rectangle.

Next, layer 3 was interpolated into a 0.0277-min grid from ETOPO2 data and updated with a navigation chart from DISHIDROS TNI AL (Indonesian Marine Corps). This chart covers depths of 3000–4000 m at a 1:100000 scale. The fourth layer was treated in almost the same way as layer 3, but in a different area and to a different extent. This layer was interpolated into a 0.0048-min grid from ETOPO3 and was updated with other navigation chart data to replace the GEBCO land elevation data used prior to its erosion.

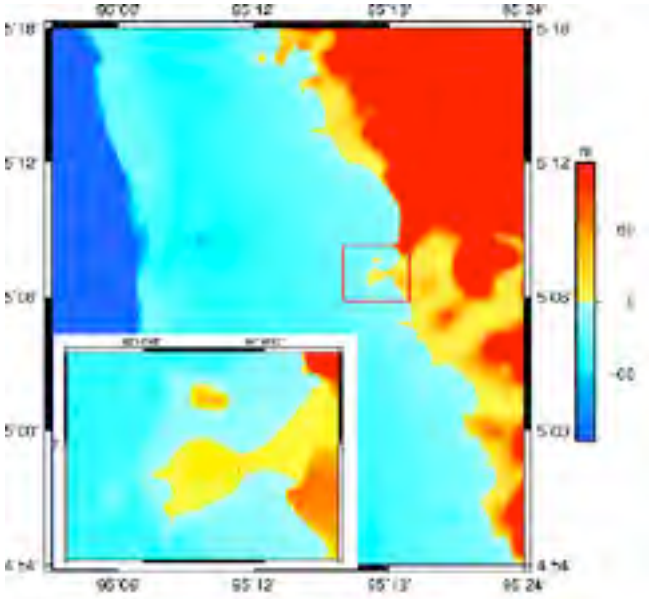

Figure 5. Layer 3 of computational domain with layer 4 marked in a red rectangle.

TABLE 1. Grid specifications for each layer.

Layer Id	extent of grid Longitude	Grid Spacing	Grid size and coordinate system	Grid size and coordinate system	Type of Shallow water equation
Layer 01	79.2–107.6	−13.6–18.1833	1 min (1851 m)	1705 × 1908 Spherical	Linear
Layer 02	94.61–97.79	3.41–6.29	0.166 min (307.266 m)	1146 × 1038 Spherical	Linear
Layer 03	95.053–95.50	4.803–5.247	0.0277 min (51.27 m)	966 × 960 Spherical	Linear
Layer 04	95.269–95.310	5.102–5.134	0.00463 min (8.76 m)	534 × 414 Spherical	Linear

3.3 Numerical Simulation

Numerical simulation was performed with COMCOT to simulate the tsunami propagation. We used the leap-frog finite difference scheme in the nested grid system to calculate both shallow

water equations (linear and non-linear). This model has been validated experimentally (Liu et al., 1995) and has been successfully implemented to investigate historical tsunami events such as the 1992 Flores Island tsunami (Liu et al., 1995) and the 2004 Indian Ocean tsunami (Wang and Liu, 2006a, 2006b, 2007).

In the nested grid system, the inner grid is adapted to a smaller size and nested inside an outer grid. Water elevation and depth-averaged velocity results are then interpolated from the larger grid into the smaller one. The larger grid contains layers 1, 2, and 3, and we used the linear shallow water equation for the grid system. Layer 4 differs from the other three layers as it comparatively smaller in size. The governing equations in the cartesian coordinate system of the non-linear shallow water equation that we used can be expressed as follows:

$$\frac{\partial \eta}{\partial t} + \frac{1}{R\cos\varphi}\left\{\frac{\partial P}{\partial \psi} + \frac{\partial}{\partial \varphi}\left(\cos\varphi Q\right)\right\} = -\frac{\partial h}{\partial t}, \quad (1)$$

$$\begin{aligned}&\frac{\partial P}{\partial t} + \frac{1}{R\cos\varphi}\frac{\partial}{\partial \psi}\left\{\frac{P^2}{H}\right\} + \frac{1}{R}\frac{\partial}{\partial \varphi}\left\{\frac{PQ}{H}\right\}, \\ &+ \frac{gH}{R\cos\varphi}\frac{\partial \eta}{\partial \psi} - f\,Q + F_x = 0\end{aligned} \quad (2)$$

$$\begin{aligned}&\frac{\partial Q}{\partial t} + \frac{1}{R\cos\varphi}\frac{\partial}{\partial \psi}\left\{\frac{PQ}{H}\right\} + \frac{1}{R}\frac{\partial}{\partial \varphi}\left\{\frac{Q^2}{H}\right\}, \\ &+ \frac{gH}{R}\frac{\partial \eta}{\partial \varphi} + f\,P + F_y = 0\end{aligned} \quad (3)$$

$$f = \Omega\sin\varphi \quad , \quad (4)$$

$$F_x = \frac{gn^2}{H^{7/3}}P\left(P^2 + Q^2\right)^{1/2} \quad , \quad (5)$$

$$F_y = \frac{gn^2}{H^{7/3}}Q\left(P^2 + Q^2\right)^{1/2} \quad , \quad (6)$$

$$H = \eta + h \quad , \quad (7)$$

where η is the water surface elevation; (P,Q) gives the volume fluxes in X (west–east) direction and Y (south–north) direction, respectively; (φ,ψ) are the latitude and longitude; R is the Earth's radius; g is the gravitational acceleration; and h is the water depth. The term $-\partial h/\partial t$ reflects the effect of transient seafloor motion; f represents the Coriolis force coefficient due to the Earth's rotation; Ω is the rotation rate of the Earth; H is the total water depth; F_x and F_y represent the bottom friction in the ψ and φ direction, respectively; and n is Manning's roughness coefficient.

4. RESULTS

The hydrodynamic forces were produced with the COMCOT simulation, which made it possible to consider the tsunami wave height and depth-averaged velocity. Furthermore, these two factors were used as input to calculate shear stress in the inundation area. The next step in the investigation of how the tsunami impact caused the land separation required the simulation of the sediment transport. Tsunami wave height was used as input data for Delft3D-FLOW. The morphological change was simulated by Delft3D-FLOW in 1 hour.

4.1 Tsunami Hydrodynamic

Land separation is caused by a number of hydrodynamic forces, including wave height and depth-averaged velocity. Wave heights were massively dispersed until reaching and inundating the land area, and they severely impacted the sediment transport by erosion and sedimentation. The COMCOT simulation results showed that the wave height at observation point 15 reached 16.054 m. This result clearly demonstrates the occurrence of overtopping in the Ujong Seudeun land bar area that connected the village to the main island.

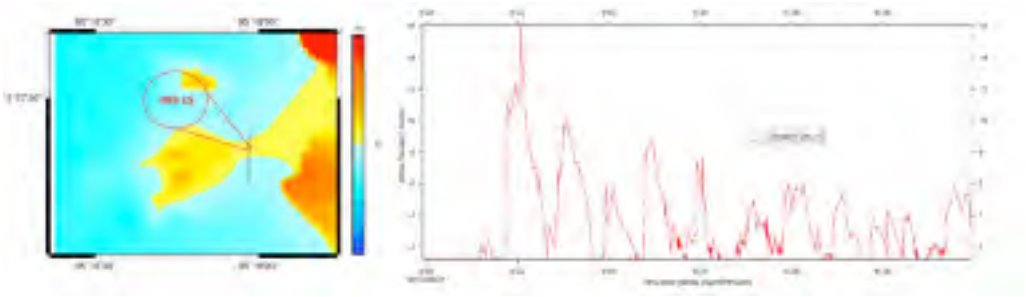

Fig 6

Overtopping occurred over a 3-hour duration in the COMCOT simulation. The highest wave came within 24 min at a height of 16.054 m, as shown in Figure 6. This event made the highest impact on the sediment transport, and the others followed to complete the hydrodynamic process. The shape of the area contributed to the overall impact, since waves that came into the area near the land bar observation point were narrower.

The COMCOT simulation results show the average maximum tsunami wave height at each observation point to be 15 m. This simulation result clearly explains how overtopping occurred numerous times since the highest elevation in the land bar area was only 4.6 m high.

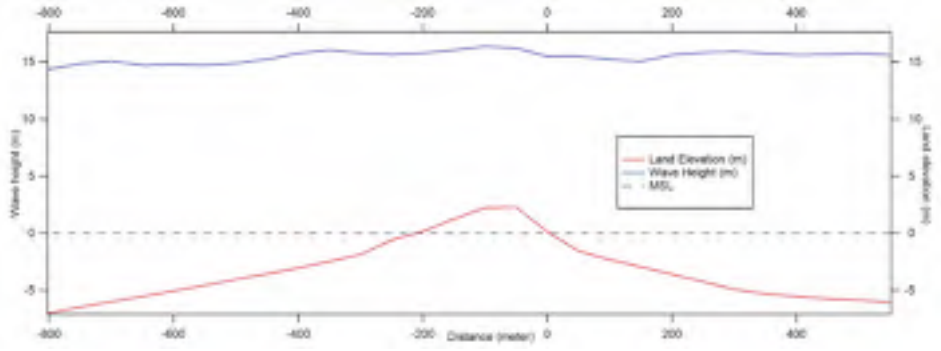

Figure 7. Maximum wave height at each observation point.

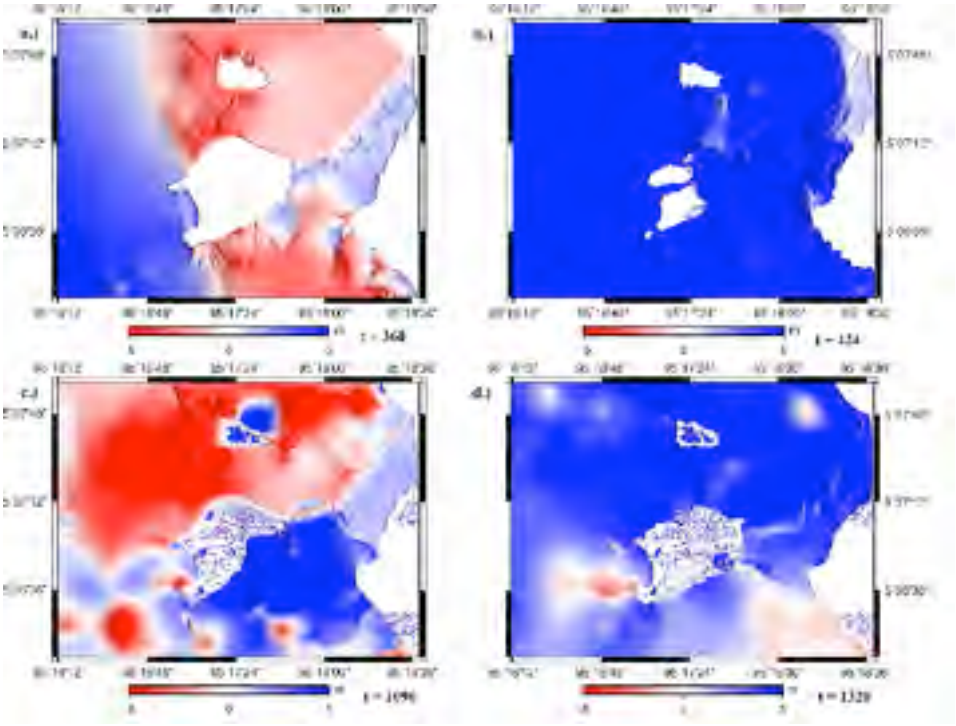

Figure 8. Tsunami dispersion in COMCOT simulation.

Tsunami waves overtopped the land several times in the COMCOT simulation, with the first wave hitting the western area of Ujong Seudeun 6 min after the earthquake. Although these first waves hit and flooded the land bar area, their impact was not great because their heights did not

reach 1 m. After 1 min and 4 sec, the waves coming from the west direction turned north on the upper side of the land bar and turned south on the lower side. As the waves met at the land bar, they merged into a higher wave but did not cause the land bar to separate from the mainland, as shown in Figures 8(a) and 8(b).

As the simulation process continued, we observed the wave suspected to have eroded the land area at 18 min and 16 sec after the megathrust earthquake. The wave came from the south of Ujong Seudeun Island and struck the land bar. At this point, the land bar began to erode but not significantly. It then continued to erode, and sediment was deposited at different locations and times. In addition, the depth-averaged velocity was high, as derived from the COMCOT simulation, with most of the wave reaching 10 m/s, and the highest velocity occurring at observation point 19 with 10.930 m/s. This high velocity contributed to the generation of a high bed shear stress, which then led to a greater capability for the flow (tsunami wave) to erode the sediment particles. Depth function is a significant aspect of the shear stress calculation, such that the shear stress produced in shallow water is bigger than that in deep areas. The depth-averaged velocity also plays an important role. It increased in the area near the land bar because the cross-section area had become smaller. The flow continued through with the same volume but through a narrower area.

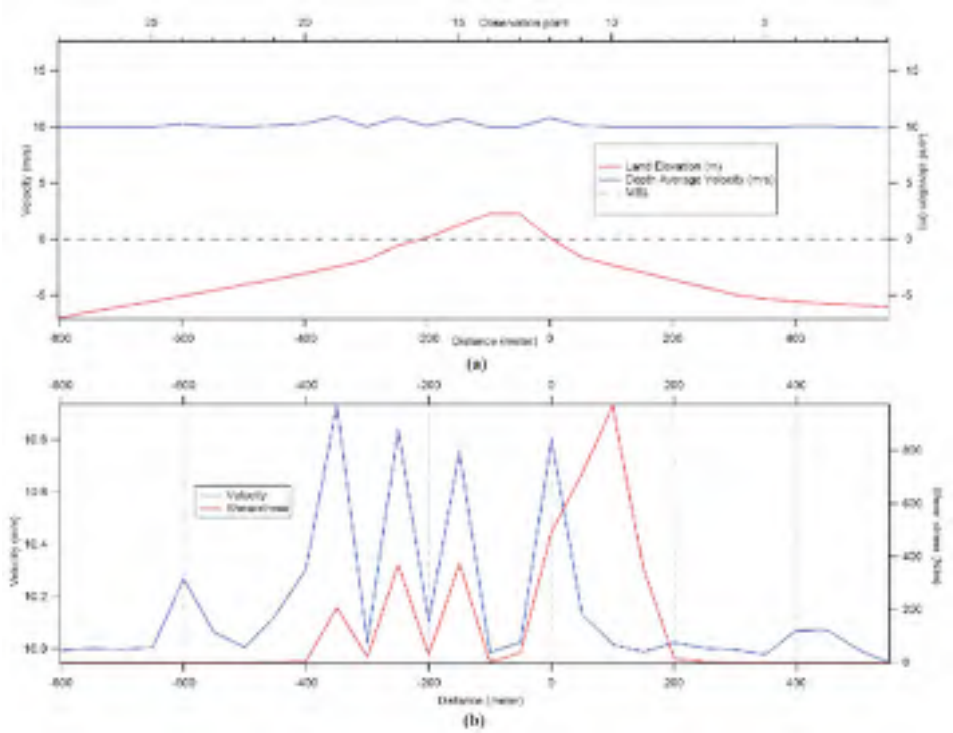

Figure 9. (a) Maximum tsunami height and (b) maximum velocity with shear stress at several observation points.

The shear stress results graphed in Figures 9(a) and 9(b) show the velocity and shear stress fluctuations and illustrate the sediment transport process as it occurred. The fluctuations of these two parameters indicate the high probability for the Ujong Seudeun land bar to be eroded and ultimately swept away. This hypothesis is confirmed in the sediment transport subsection.

4.2 Sediment Transport

Sediment transport requires hydrodynamic forces capable of moving sediment particles. A significant change in water elevation will produce a strong and high velocity that will affect particle movement on the sea bed. Tsunami waves produce a massive volume of sea water by changing the characteristics of an area, consequently generating a high and variable depth velocity. The depth velocity produced in the 2004 Indian Ocean tsunami was high enough to make a huge impact, affecting wave heights and water volumes, as well as the bathymetry. As happened in Ujong Seudeun, the COMCOT simulation results show that wave heights reached 16.054 m, which is more than sufficient to significantly impact the sediment transport process.

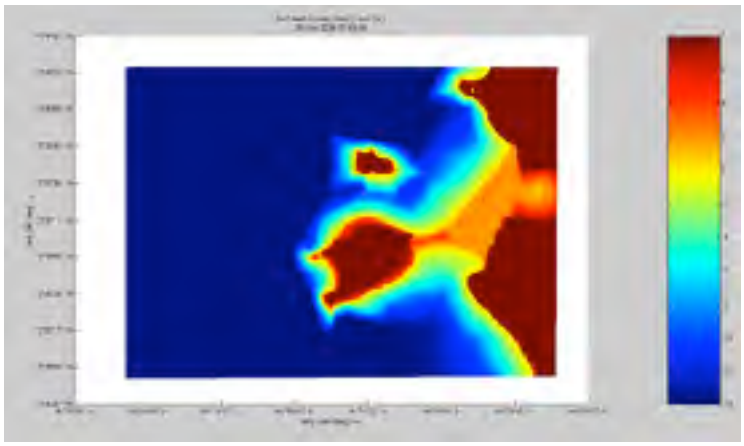

Figure 10. Simulation area on Delft3D-FLOW.

We used Delft3D-FLOW to simulate the sediment transport process during a 1-hour tsunami simulation using COMCOT layer 4, as shown in Figure 10. The hour-long Delft3D_FLOW sediment transport simulation showed very clearly that the land bar was eroded due to the tsunami waves. We ran the Delft3D-FLOW simulation using COMCOT's tsunami waves and layer 4 elevation as input data.

The Delft3D-FLOW simulation results were nearly identical to those of the COMCOT simulation. The real erosion impacts, as seen in the COMCOT simulation, started 21 min after the simulation began (at 08:22 am local time). The wave came from the north and seemed like a back wave from the northern area because the rupture sources were from the western area. The waves were continuous until the land bar completely separated after 44 min (08:43 am local time). Waves that came from the south, west, and north brought a high speed current that caused sedimentation

and erosion in some areas and at various times. Elevation changes were recorded by the observation points on the land bar in the Delft3D simulation process. There were 14 observation point on the land bar area, but only five were used to represent the sediment transport process, including obs 5, 6, 11, 12, and 13.

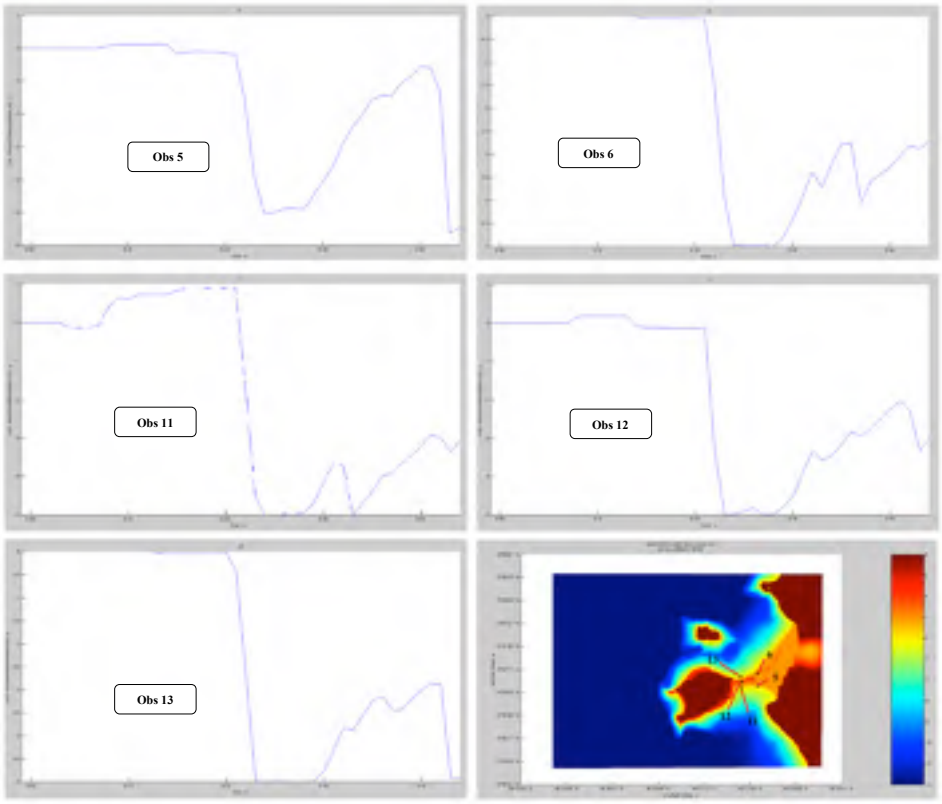

Figure 11. Simulation graphic of sediment transport process at several represented observation points.

The sediment transport process revealed by these 5 observation points represents the erosion process as observed by Delft3D. Each of the observation points illustrate the sediment transport accumulation process, and all five observation points show that the erosion process began 22 min after the earthquake. The tsunami waves continuously eroded the land bar and produced an area averaging 3.2 m in depth. This happened because the beach morphology and Keluwang Island near Ujong Seudeun trapped the waves and amplified their effect. The amplification became sufficiently large to erode the entire land bar area and leave Ujong Seudeun as a completely separate island in Aceh Jaya.

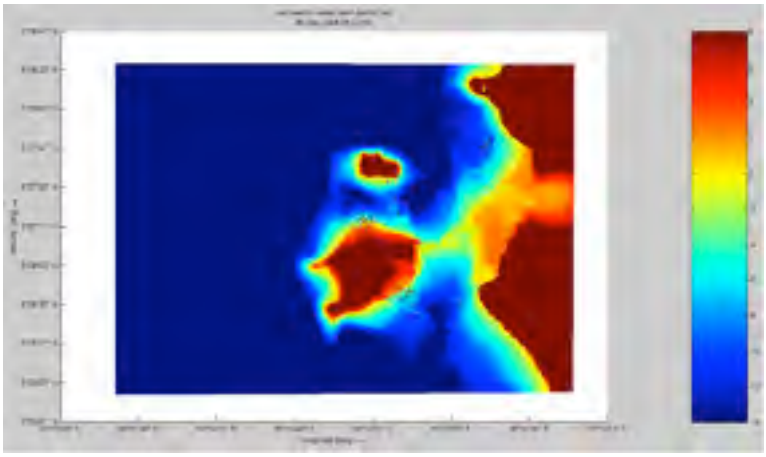

Figure 12. Simulation area 23 min after hit by tsunami wave.

Author 6/5/15 7:57 AM
Comment: Remark: Please verify if this should be 22 min.

5. CONCLUSIONS

The efficient investigation of the land separation impacts of a tsunami (sediment transport process) requires a numerical simulation approach. In this study we observed two events—the tsunami propagation and the sediment transport process. We simulated these two events continuously using two different software tools. The tsunami propagation was simulated with COMCOT and the sediment transport process was simulated with Delft3D-FLOW. The COMCOT simulation was performed with GEBCO data and available navigation charts, and the simulation results were then used as input data for Delft3D-FLOW to observe the sediment transport prosess on the land bar that connected Ujong Seudeun to the main island. The COMCOT simulation results show that the tsunami waves had a massive impact on the land separation in Ujong Seudeun. This impact was confirmed by the Delft3D-FLOW simulation results. The land bar that connected Ujong Seudeun with the main island began to erode 22 min after the earthquake occurred, and it separated completely after another 22 min. These processes explained the tsunami's huge impact on the erosion of the land until it separated as well as how the separation occurred. These results also demonstrate that COMCOT and Delft3D-FLOW can be coupled to model tsunami sediment transport.

ACKNOWLEDGMENTS

The authors are grateful to USAID and the National Academy of Sciences who funded this research through PEER Cycle 3, Sponsor Grant Award Number: AID-OAAA-A-11-00012 and Sub Grant Number PGA-2000004893 with the research project title: Tsunami Waves Impacts on Coastal Morphological Changes Based on Sediment Transport Simulations.

REFERENCES

1. Deltares (2007) Deltares, User Manual Delft3D-Flow: Simulation of Multi-Dimensional Hydrodynamic Flows and Transport Phenomena, Including Sediments (Delft, The Netherlands).
2. Jaffe B, Gelfenbuam G (2007) A simple model for calculating tsunami flow speed from tsunami deposits. Sediment Geol 200(3–4):347–361
3. Moore A, Nishimura Y, Gelfenbaum G, Kamataki T, Triyono R (2006) Sedimentary deposits of the 26 December 2004 tsunami on the northwest coast of Aceh, Indonesia. Earth Planets Space 58(2):253–258
4. Richmond B, Szczucin´ski W, Chague´-Goff C, Goto K, Sugawara D, Witter R, Tappin DR, Jaffe B, Fujino S, Nishimura Y, Goff J (2012) Erosion, deposition and landscape change on the Sendai coastal plain, Japan, resulting from the March 11, 2011 Tohoku-oki tsunami. Sediment Geol 282:27–39.
5. Shi S, Dawson AG, Smith DE (1995) Coastal sedimentation associated with the December 12th, 1992 tsunami in Flores, Indonesia. Pure and Applied Geophysics 144(3–4):525–536
6. Vatvani, D., Van Veen, B. A. D. And Zijl, F (2012) Tsunami flood modeling for Aceh and West Sumatra and its application for an early warning system. Continent. Shelf Res.
7. Wang, X., Liu, Philip L-F (2006a) An analysis of 2004 Sumatra earthquake fault plane mechanisms and Indian Ocean tsunami. Journal of Hydraulic Research 44 (2):147–154
8. Wang, X, Liu, Philip L-F (2006b) The 2004 Indian Ocean Tsunami: Inundation Simulation at Trincomalee, Sri Lanka, Internal report (Personal communication)
9. Wang, X, and Liu, Philip L-F (2007) Numerical simulations of the 2004 Indian Ocean tsunamis: coastal effects. Journal of Earthquake & Tsunami 1(3):273–297
10. Borsje, B.W. et al., Modeling large-scale cohesive sediment transport affected by small-scale biological activity, Estuar. Coast.Shelf Sci. (2008), doi:10.1016/j.ecss.2008.01.009

ISSN 8755-6839

SCIENCE OF TSUNAMI HAZARDS

Journal of Tsunami Society International

Volume 34 Number 3 2015

COASTAL RISK IN THE ALGIERS REGION (ALGERIA): INSIGHTS FROM TSUNAMI VELOCITIES, SEISMIC GROUND MOTION AND REMOTE SENSING

L. A. Amir[1,*], A. Dahlab[1], M.B. Douaifia[1]

[1] *USTHB-FSTGAT, Department of Geophysics, BP 32, 16111 Bab Ezzouar, Algiers, Algeria*

B. Theilen-Willige[2]

[2]*Institute of Applied Geosciences, Berlin University of Technology (TU Berlin), Berlin, Germany*

ABSTRACT

The Algiers region (Algeria) is exposed to destructive earthquakes that sometimes trigger tsunamis. In this paper, we present an interdisciplinary approach that identifies the locations prone to related induced damage for a worst-case scenario off Algiers. Firstly, a tsunami modeling for a 7.6 earthquake in the Khair Al Din Bank is computed with the Geoclaw package. The simulation indicates that the maximum values for the surface heights are about 1.5 meters and 40 to 60 m/s for the flow velocities. Seismic shaking maps are computed as well using the OpenSHA application for the same earthquake scenario. The results show that the peak ground accelerations and peak ground velocities are the highest in the Algiers massif, which means that this area is the most exposed to a high level of infrastructural damage. Finally, the use of remote sensing and GIS applications helped to generate a susceptibility to flooding hazard map for the bay of Algiers. This approach showed that the central and the eastern part of the bay have the higher susceptibility degree to flooding.

Key Words: *Tsunami, ground motion, Algeria, flow velocities, surface heights, Algiers.*

Vol. 34, No. 3, page 173 (2015)

1. INTRODUCTION

Tsunami hazard in the Algerian coast is related to earthquakes with epicenters located offshore the western Mediterranean margin or to slides due to the numerous canyons evidenced from geophysical marine surveys (Yelles-Chaouche, 1991; Domzig et al., 2006). Several coastal cities have been destroyed in the past by coastal and offshore earthquakes. Minor to moderate tsunamis occurred in the past and have been as well reported in numerous papers with information as for the extent of the coastal inundation induced or triggered observed sea-waves. A series of boulders have been found and measured in the Algerian coast from Tipaza to Dellys (Maouche et al., 2009). The transportation of these boulders suggests catastrophic events that hit the Algerian coast. Dating (Carbon 14) and sedimentary and morphological analysis of the boulders provided quantitative data as for (1) the potential source (historical and past earthquakes) and (2) the water height necessary to displace these marine deposits (Maouche et al., 2009). All the calculations used to evaluate the physics of boulder movement were based on Nott's equations that only focused on the wave heights. However, these equations have been revised and new hydrodynamic equations have been proposed and applied for boulder transport from the flow velocity (Nandasena et Tanaka, 2013).

Hydrodynamic equations for tsunami modeling are based on the mass and momentum conservation laws. Tsunami processes involve three main steps that are (1) the generation, (2) the propagation, (3) the shoaling on the coast usually with debris transportations. Water waves' amplitude depends on the bathymetry so that when reaching the coast, tsunami waves increase in height. When flooding the coast, the waves impact the roads, houses and carry debris with such strength that the assessment of tsunami hazard and risk has to be completed with data on the energy and the flow velocities.

In this paper, an interdisciplinary approach to evaluate the tsunami and the associated / related earthquake risk for the Algiers region is presented. The Algiers bay and the central part of Algeria are regularly marked by moderate shallow earthquakes. Located at the limit between the African and the European convergent plates, the earthquakes sometimes reach magnitude above 6 and trigger tsunami waves and turbidity currents. The second section of this paper presents the materials and methods used to evaluate the tsunami hazard from tsunami modeling for a structure identified by previous studies as a potential source for a major event off Algiers. The simulation output provides with surface heights and flow velocities for a series of points of interest in the studied area. A ground motion analysis (seismic) is also developed to discuss on the ratio tsunami versus earthquake risk. A remote sensing and a GIS application are as well included as a combined approach to investigate the exposure to flooding and risk for the studied region. The third section presents the results obtained. Finally, the fourth section discusses on the research output here investigated for coastal risk assessment and exposure related to vulnerability and susceptibility to flooding.

2. MATERIALS AND METHODS

2.1 The tsunamigenic scenario for Algiers

The highest seismogenic potential in the Algiers Bay is related to the Sahel Fold and anticline

(inland) and the Khayr al Din Bank (KDB) (offshore, in the Neogene margin) (Yelles et al., 2009; Heddar et al., 2012). In this study, the potential source for tsunami generation is considered to be associated to the co-seismic vertical uplift of the sea bottom in case of an important earthquake with an epicenter at the foot of the KDB where a reverse active fault has been identified and mapped from marine geophysical surveys (Domzig, et al., 2006; Yelles et al., 2009).

Due to the collision between the African and the European tectonic plates, the Algiers region is under a compressive regime with a stress field oriented NNW-SSE. The active structures mapped in the margin, off NW of Algiers, strike in the E-W and NNW-SSE directions. The strike angle varies between 60˚ to 70˚ (Domzig, et al., 2006; Yelles, et al., 2009). The MARADJA cruise provided accurate maps showing the margin's strike changes abruptly from the Algiers Massif with an E-W direction in the eastern part of the Massif and a NW-SE direction in the western part. Yelles et al. (2009) also indicated that from east near Tamentfoust to west near Ain Benian, the margin depicts first a roughly 60˚E and E-W direction. Active seismogenic structures in the Algiers region extend over 70 to 80 km in length (Domzig et al., 2006; Yelles, et al., 2009; Heddar et al., 2012). In particular, the KDB is about 80 km long in a W-E direction, from the front of the Algiers massif to the north west of Cherchell. It depicts an overall E-W direction with a major change in a NW-SE direction in its eastern tip off Ain Benian (Yelles et al., 2009).

Using the seismological empirical laws, a magnitude of 7.6 is expected in the region. The Khayr al Din fault-related fold located at the foot of the margin is a blind reverse fault dipping in the southward direction. The authors agree on considering a mean dip for the fault of 47 +/- 7˚ (Yelles et al., 2009). Length and width for the fault geometry can be estimated from empirical relationships. Consequently, in this work we assume a width of 29.3 km and a length of 73.3 km for the tsunami source. The epicenter is here located at 2.98E, 36.98N and the focal depth is 07 km. Finally, and the amount of slip in the program was suggested from past destructive earthquakes related to blind reverse faulting. In 1980, the El Asnam earthquake (Ms = 7.3) revealed the existence of a reverse blind fault and produced surface faulting in the Chelif basin (Yielding, 1985). The field studies carried out in the epicentral area identified three main thrust segments with distinct co-seismic slip values. Yielding (1985) reported the vertical displacement reached a maximum of about 5 m near the central part of the fault, though averaged about 2 – 3 m. This allows us to propose a mean value of 3.5 meters for the dislocation in the present study.

2.2 Methodology

2.2.1 The hydrodynamic modeling

Tsunami waves are long water waves with three distinct phases from the generation to the impact on shorelines. Tsunami waves' propagation is expressed using the conservation laws for mass and momentum. The shallow water equations solved by the Geoclaw package describe any of the diverse flow regimes from the global domain to more near field complex areas in the shoreline or onto dry land (George and Leveque, 2006). The set of equations include flows that defined a hyperbolic system for tsunami modeling. The Geoclaw package was developed to solve the integral conservation law for mass and momentum from a finite volume method based on the Riemann numerical solutions approach (George and Leveque, 2006). The set of equations include flows that defined a hyperbolic system for tsunami modeling. The Riemann solver for the tsunami

modeling can then be written by the equation hereby (eq.1) (George & Leveque, 2006):

$\boldsymbol{q}t + A\,\boldsymbol{q}\boldsymbol{q}x = 0$ *(eq. 1)*

Where $\boldsymbol{q} = (h,\ hu\ ,12gh2+hu2,b)T$ and $A \in \mathbb{R}4*4$, h is the water depth, u is the horizontal velocity, g is the gravitational constant and b is the bottom surface elevation.

In this work, the manning coefficient was set to 0.025 for depths lower to zero and 0.06 for dry land modeling. The time step was 05 minutes and the duration of the modeling was set to 02 hours. The topography was extracted from the ETOPO 1 arc - minute custom grid data (Amante & Eakins, 2009). The grid extends from 0˚E to 8˚E for the longitude and 36˚N to 44˚ N for the latitude (Figure 1).

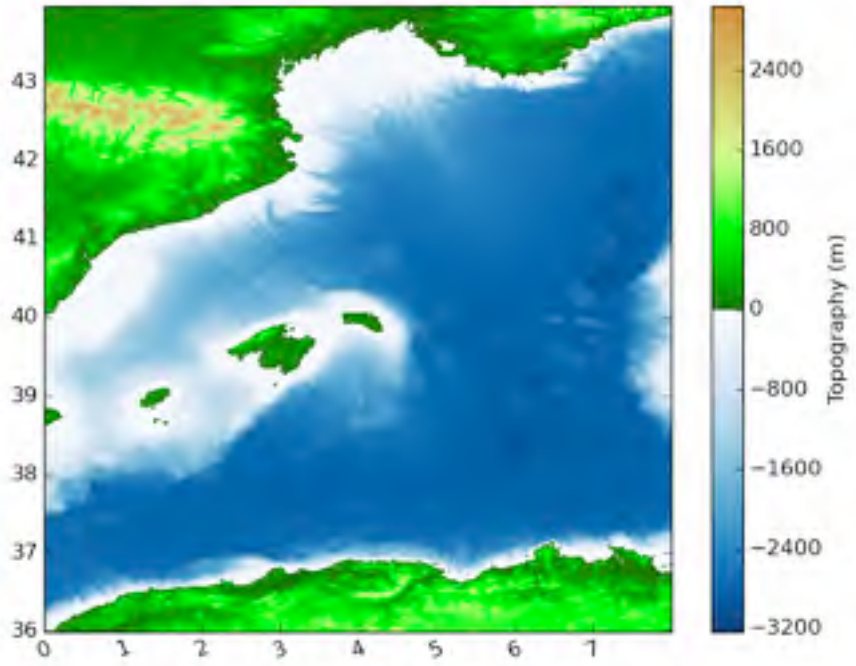

Figure 1: Topography of the West Mediterranean – source: ETOPO 1mn (NGDC-NOAA).

2.2.2 The ground motion

Earthquake damage can be evaluated through seismic hazard analysis and the modeling of the ground motion. Many studies on loss estimations for urban cities rely on the peak ground acceleration data provided either from seismic records or from numerical modeling (Field et al., 2005; Field et al., 2005). In this work, the interdisciplinary approach to evaluate the coastal risk for the Algiers region involves the presentation of the earthquake shaking maps computed from the OpenSHA application (Field et al., 2005).

Peak ground accelerations and peak ground velocities are estimated using an earthquake scenario and the appropriate attenuation law/relationships. The earthquake source introduced in the OpenSHA application can either be a fault segment or a single point representing the assumed

hypocenter. In this work, the Abrahmson and Silva attenuation law (Abrahamson et Silva, 1997) is selected. This relationship has been set up for a large series of earthquake around the world and therefore, is one of the most general attenuation laws. The earthquake source considered is one single point rupture. The hypocenter introduced in the model is the one considered for the tsunami modeling with the Geoclaw software. The seismological parameters introduced in the application are those considered for the tsunami modeling with the Geoclaw package.

2.2.3 Remote sensing for flooding hazard assessment

Airborne and space borne remote sensing systems and image analysis techniques have been developed to an extent where civil and commercial earth observation instruments can contribute significantly to supporting the management of major technical and natural disasters as well as humanitarian crisis situations. Open-source tools as OpenStreetMap or Google Earth were used for gaining the necessary information, as well as evaluations of classified satellite imageries and further Web-tools. GoogleEarth-data were evaluated in Quantum-GIS. Satellite data downloaded from the Global Land Cover Facility, University of Maryland and the EarthExplorer of the USGS / USA contributed to the geodatabase. A RapidEye-satellite imagery of Algiers was provided by BlackBridge, Berlin / Germany. Free Open Source Software (FOSS) such as LEOWorks provided by ESA and Quantum-GIS (GNU General Public License) were applied additionally to ArcGIS / ESRI and ENVI / EXELIS digital image processing software. This data mining is aiming at visualizing critical areas and providing information about damage in case of emergency due to flooding hazards as fast as possible, as the civil protection units need this information for their management. The almost actual inventory of land use and infrastructure (bridges, railroads, roads, river embankments, etc.), industrial facilities and the structure of settlements and cities (considering age, structure and function of buildings) is an important issue for the hazard assessment and damage loss estimation. Digital image processing using software was used not only for the enhancement of RGB-imageries, but also to derive water index (NDWI—Normalized Difference Water Index) and vegetation index (NDVI Normalized Difference Vegetation Index) images. Another important digital processing method applied in this study was the supervised and unsupervised image classification. In urban areas the inventory of building stocks, built-up density, building heights, infrastructure, or undeveloped areas is relevant to the vulnerability identification and quantification.

For the detection of water currents in the Bay of Algiers various image-processing procedures were tested and the results combined with available wind information. Evaluations of LANDSAT satellite imageries in time series contribute to a better knowledge of water current dynamics, influenced among other factors (wind direction and speed, etc.) by the coastal morphology.

Morphometric properties and disposition of coastal areas can influence to a great extent the susceptibility to flooding due to flash floods, storm surge, meteo- or tsunami waves The systematic inventory of morphometric properties according to a standardized GIS-approach based on digital elevation data and evaluations of satellite imageries from flooding prone areas contribute considerably to the detection of areas, that are more susceptible to flooding due to their geomorphologic disposition. It offers a low-cost to no-cost approach (as the used DEM data are free), that can be used in any area, providing a first basic data stock for emergency preparedness by providing susceptibility-to-flooding maps.

The term susceptibility does not predict when a hazard will occur. The susceptibility assessment derives places, which are exposed to flooding hazards due to their morphologic disposition. The factors influencing the flooding susceptibility are classified into causal and triggering. The causal factors determine the initial favorable conditions for the occurrence, while the triggering factors such as high precipitation rates or storm surge principally determine the timing. Causal factors are, among others, the slope gradient, curvature, lithology and groundwater table level. The triggering mechanisms are quite unpredictable, as they vary in time and their composition. The percentage of influence of one factor also changes in consideration of seasonal and climatic factors. In very hot and dry seasons the risk of flooding to flash floods is generally lower than in wet seasons with higher precipitation occurrence. Some of these causal factors can be integrated as layers into a GIS. Therefore, based on DEM data morphometric maps were created and terrain parameters were extracted such as shaded relief, aspect and slope degree, minimum and maximum curvature or plan convexity maps using ENVI and ArcGIS software as well as Quantum-GIS. The morphometric parameters such as lowest height level, lowest slope degree, amount of flow accumulation and minimum curvature provide information of the terrain inundation susceptibility.

3. RESULTS

3.1 The tsunami modeling for the KDB Scenario (Algiers region)

The tsunami modeling was computed from the Geoclaw package (George and Leveque, 2006). The code includes a subroutine that calculates the seafloor deformation using the Okada theory for a half-space (Okada, 1992). The results show that a single fault segment off North of Algiers (Length*Width = 73.3 km*29.9 km) with a slip of 3.5 meters produces a maximum seafloor uplift deformation of about 1.6 meters (Figure 2).

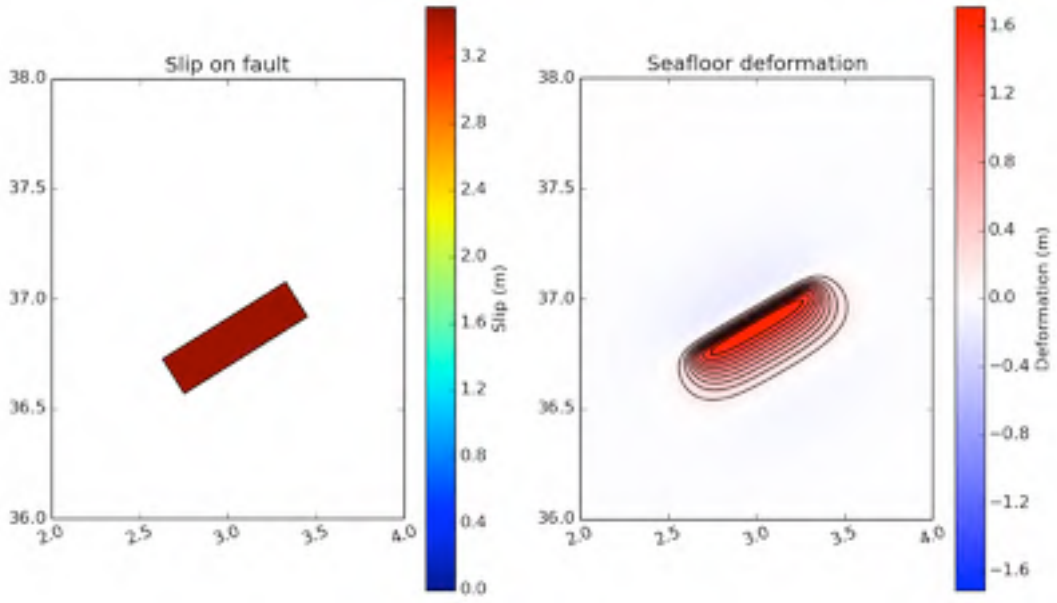

Figure 2: Co-seismic slip (meters) (2a) and Sea-bottom deformation (meters) (2b) (vertical uplift) simulated for a 7.6 magnitude earthquake, off Algiers

In this work, we present the surface height and the horizontal velocities simulated for a series of gauge/ points of interest located along the Algiers coast (see Table 1).

Table 1: Location of the points of interest for the Algiers region

ID Point of Interest	Latitude (˚N)	Longitude (˚E)
Gauge 1	1.48	36.53
Gauge 2	2.81	36.7
Gauge 3	3.1	36.95
Gauge 4	3.64	36.83
Gauge 5	3.1	36.85
Gauge 6	3.2	36.88

Figure 3 displays the tsunami propagation after five and ten minutes after the onset of the earthquake. The results show the immediate decrease of the sea in the central part of North Algeria. After five minutes, the surface heights here depicted reach above 1.5 meters in the Bou Ismail Bay and northward the epicentral zone (Figure 3a). The rising of the sea is as well shown for the gauges along the Algiers bay. Ten minutes after the onset of the earthquake, the water surface disturbance covers a larger area and water waves seemed to be trapped in both bays (rising / decrease, water flow) (Figure 3b).

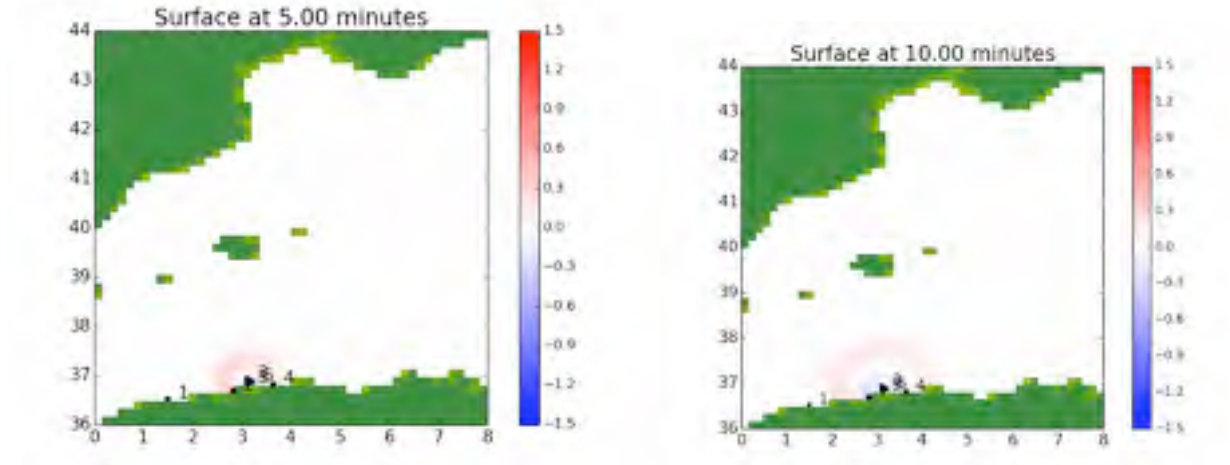

Figure 3: Tsunami propagation 05 minutes (3a) and 10 minutes (3b) after the onset of the earthquake.

The figure 4 presents the water heights simulated for the six gauges in the Algiers region. Water heights above one meter are obtained for gauge 2, 5 and 6. These three points of interests are located precisely nearby the epicenter. At gauge 1, the water height never exceeds 0.2 meters. At gauge 3, the instantaneous rising of the sea is as well simulated but is lower than what is observed closer the Algiers coast (0.8 meter). At gauge 4, the maximum water surface estimated is lower than 0.5 meter.

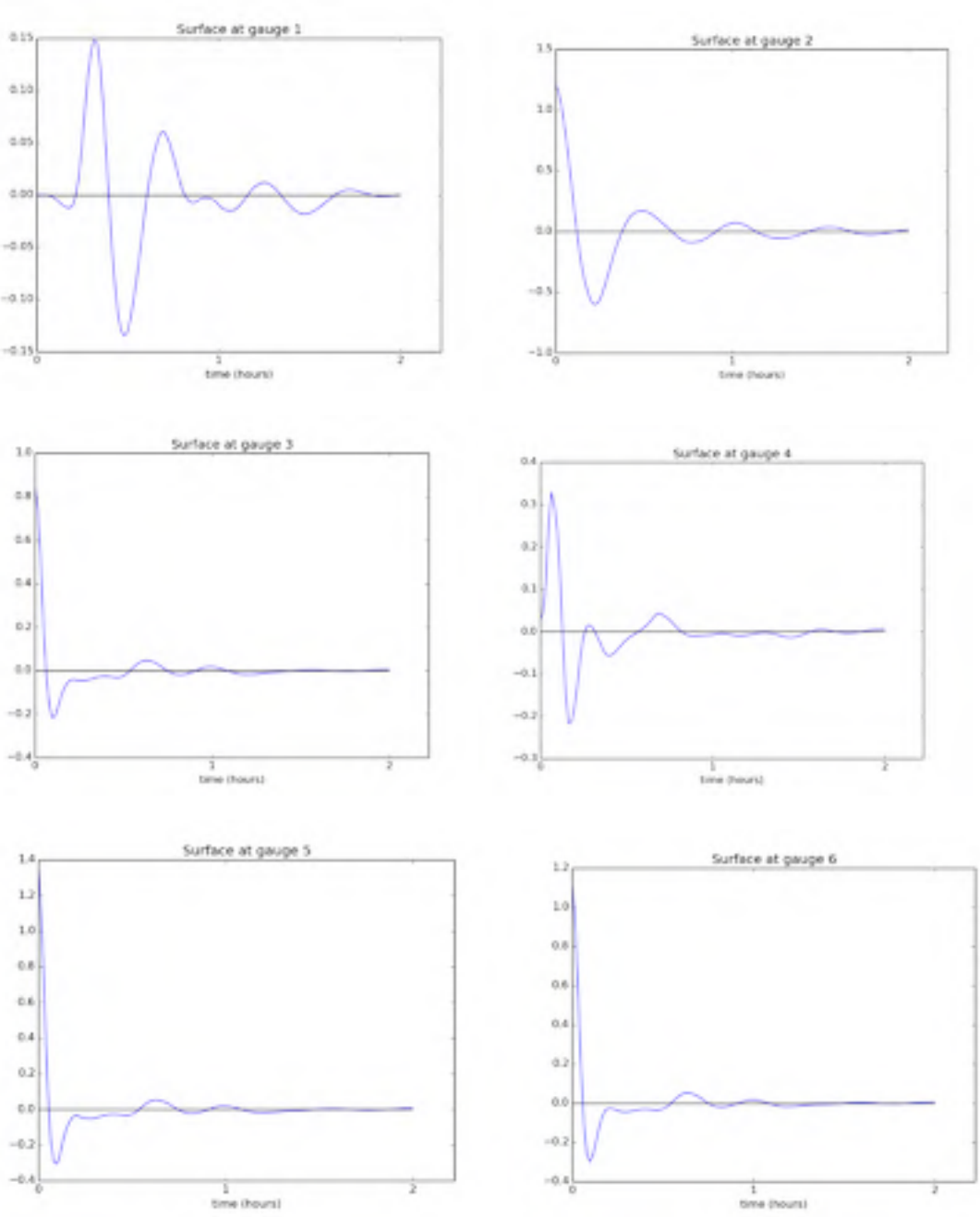

Figure 4: Water heights (meters) simulated with the GeoClaw package for the 6 points of interests in the Algiers region.

Figure 5 depicts the flow velocities computed for gauge 2, 3, 4, 5 and 6. Both horizontal velocities are here presented (m/s). The results show that the v component (Oy direction) is higher than the u component (Ox direction) for all the gauges. The highest value for the u component is obtained for the gauges 2 and 4. The maximum values are above 20 m/s. The highest value for the v component is obtained for gauge 3 with 60 m/s. The lowest value for the v component is for gauge 4. Comparable velocities are estimated for both gauges 5 and 6 with about 10 m/s for the u component and about 40 m/s for the v component.

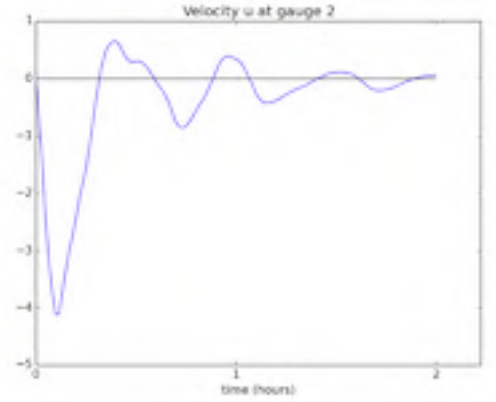
Velocity u at gauge 2
time (hours)

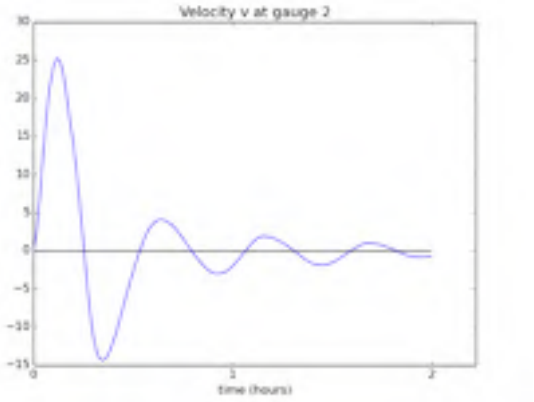
Velocity v at gauge 2
time (hours)

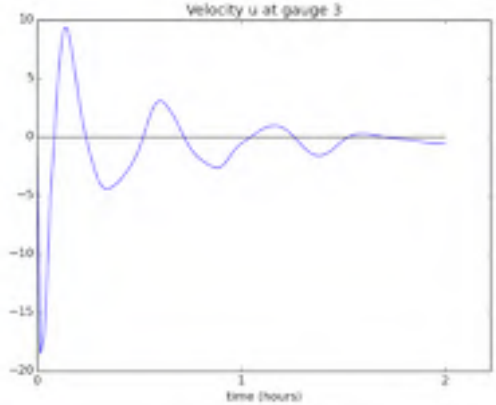
Velocity u at gauge 3
time (hours)

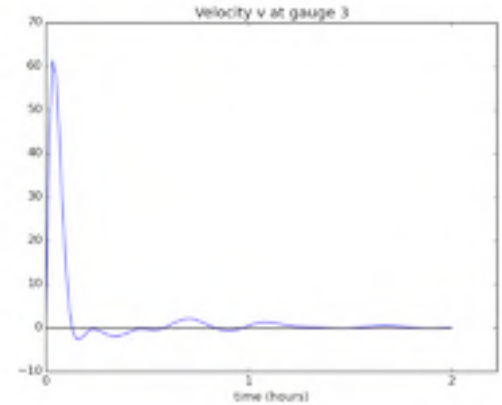
Velocity v at gauge 3
time (hours)

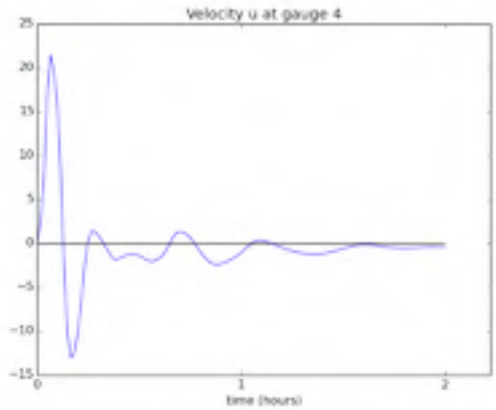
Velocity u at gauge 4
time (hours)

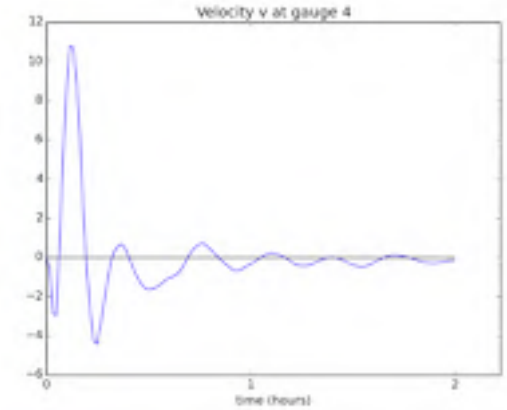
Velocity v at gauge 4
time (hours)

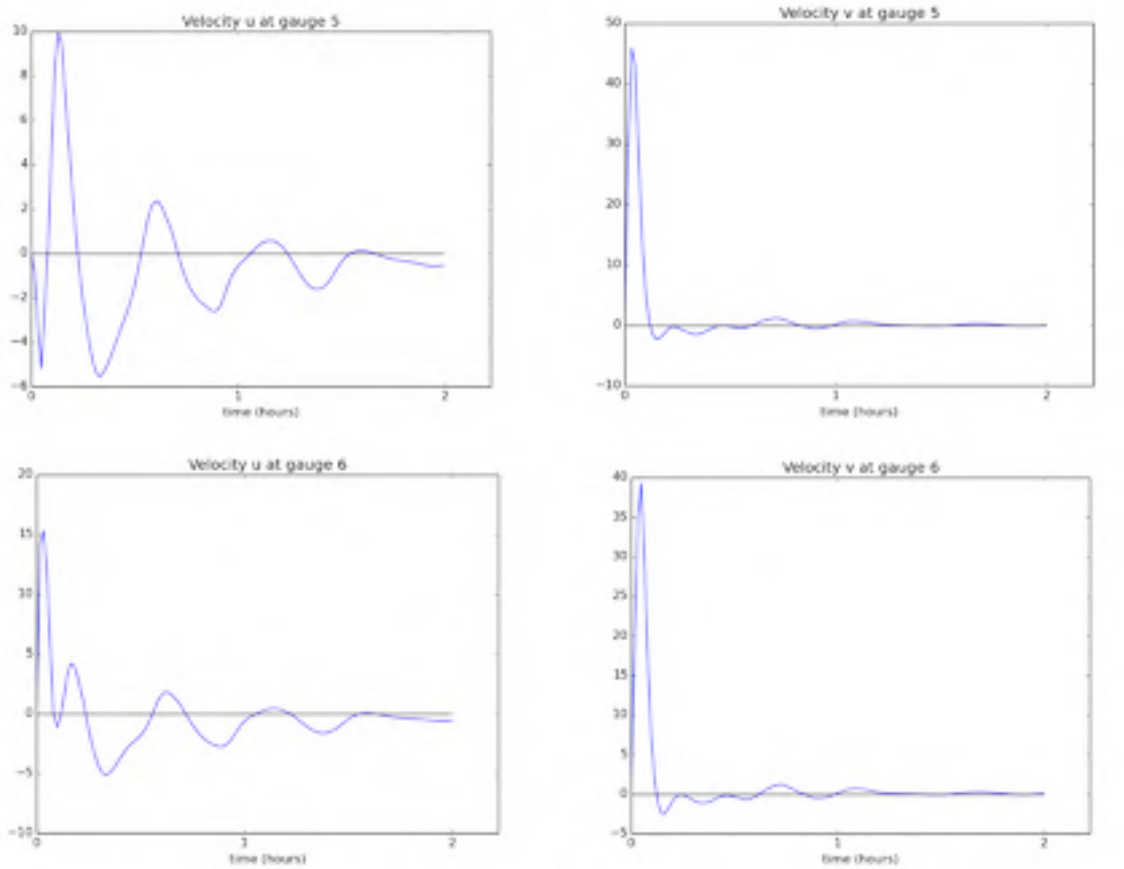

Figure 5: Flow velocities (m/s) computed with the Geoclaw package for gauges 2, 3, 4, 5 and 6.

3.2 The ground motion modeling for the KDB Scenario (Algiers region)

The KDB earthquake shaking maps were produced from the OpenSHA application for a single point rupture that represents the hypocenter off NW of Algiers. The results here presented indicate the level of the peak ground accelerations and the peak ground velocities. Both type of data help to evaluate the areas prone to infrastructure damage along the bay of Algiers and the bay of Bou Ismail and the coastal risk related to the earthquake. The ground shaking levels for the Algiers region shows the dependency on the earthquake location.

The peak ground accelerations (PGA) are shown in the figure 6. The results indicate the highest PGA values are 0.4g – 0.5 g (or 3.924 m/s^2 – 4.905 m/s^2). These are obtained for the western part of the bay of Algiers. The lowest values are simulated for the western part of the Bou Ismail bay (less than 0.15 g, or 1.47 m/s^2). The ground motion modeling indicates the highest seismic risk for an earthquake located off Algiers (2.98E, 36.98N) is for the Algiers Massif (Figure 6). The figure 7 represents the peak ground velocities (PGV) simulated for the same scenario. The highest values for the PGV are distributed in the Algiers Massif (between 35 to 50 cm/sec.). Along the Algiers bay, the values range between 28 to 37 cm/sec. Along the Bou Ismail bay, the velocities are lower and are less than 22 cm/s.

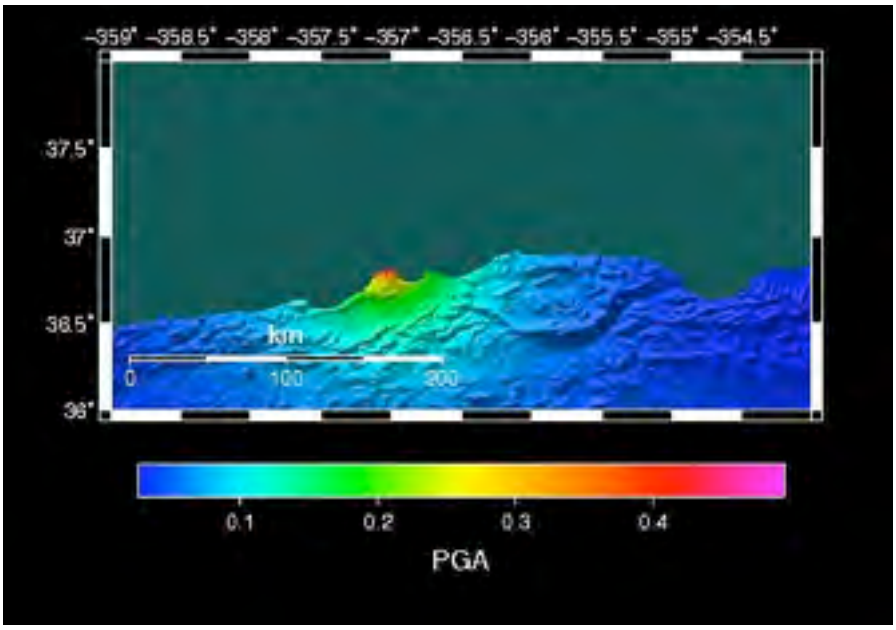

Figure 6: Peak Ground Accelerations (g) simulated for a 7.5 earthquake off Algiers region with the OpenSha application

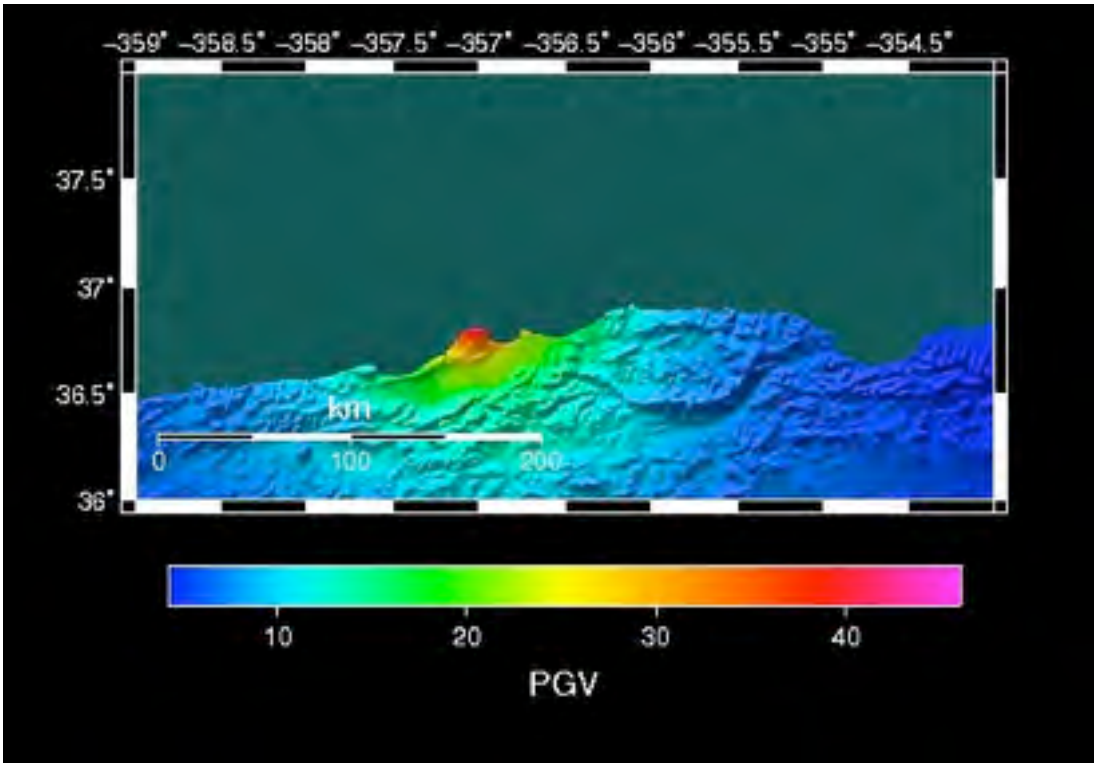

Figure 7: Peak Ground Velocities (cm/sec) simulated for a 7.5 earthquake off Algiers region with the OpenSha application.

Digital Image Processing in the Algiers Bay

Evaluations of LANDSAT and RapidEye imageries clearly show nearly circular currents in the Bay of Algiers. This is visible on the LANDSAT scenes in Figure 8 and the RapidEye scene in Figure 9.

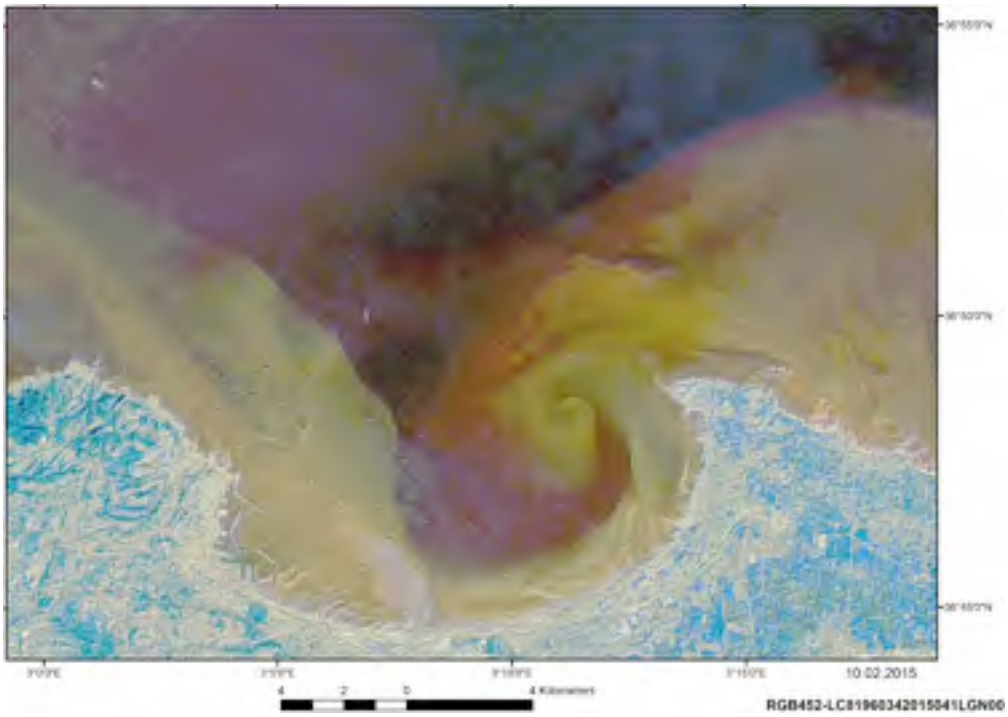

Figure 8: LANDSAT scenes in the Algiers bay

This is visible on the LANDSAT scenes in Figure 8 and the RapidEye scene in Figure 9.

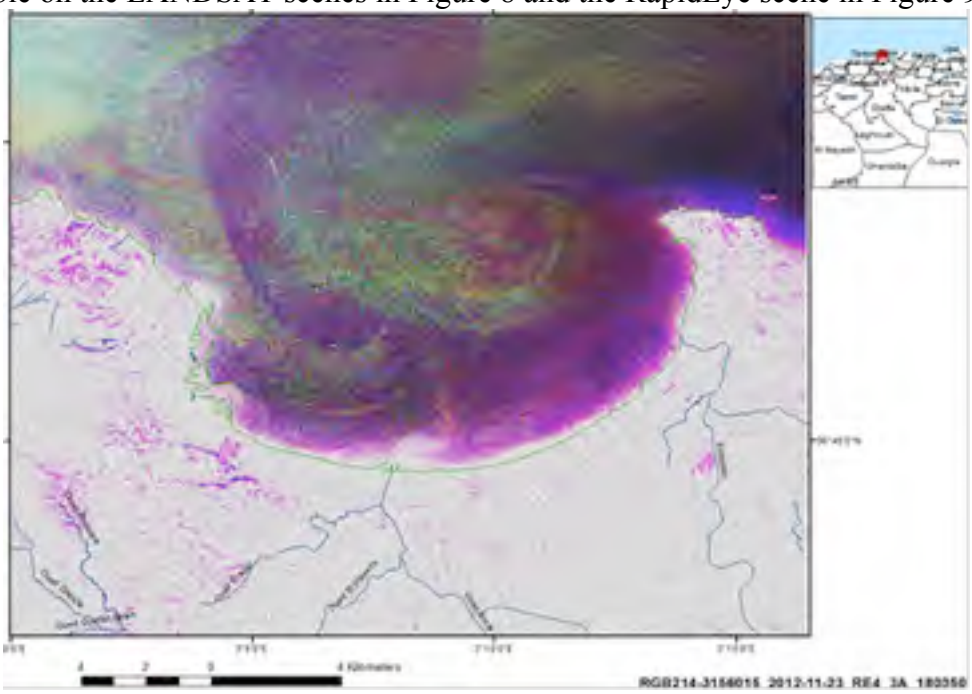

Figure 9: RapidEye scene in the Algiers bay

The development of the nearly circular shaped Bay of Algiers could be explained by such circular streaming dynamics of the water with the consequence of erosional effects. The sea surface-streaming pattern as visible on the Landsat- and RapidEye-scenes of the Bay of Algiers (visualizing the situation only of the upper centimeters) is mainly influenced by the wind situation at the acquisition time, further on by the tidal situation and the input of river water. In case of stronger tsunami events with several tsunami wave fronts circular currents cannot be excluded to occur in the Bay of Algiers as well and, thus, amplify the intensities by interfering and superimposing of incoming waves. The direction and angle of incoming, high energetic flood waves will have a great influence on the currents and dynamics. River mouths are forming an entrance for intruding water waves from the sea. Therefore, even in longer distances from the seaside flooding might be possible affecting the city area of Algiers.

The Figure 10 presents the results of the weighted overlay based on morphometric, causal factors in the area of Algiers showing those areas susceptible to flooding due to the aggregation of causal, morphometric factors. The ASTER DEM derived drainage pattern and the weighted overlay results, presented together with the sealed areas of Algiers contribute to a better visualization of urban areas susceptible to flooding (Figure 10).

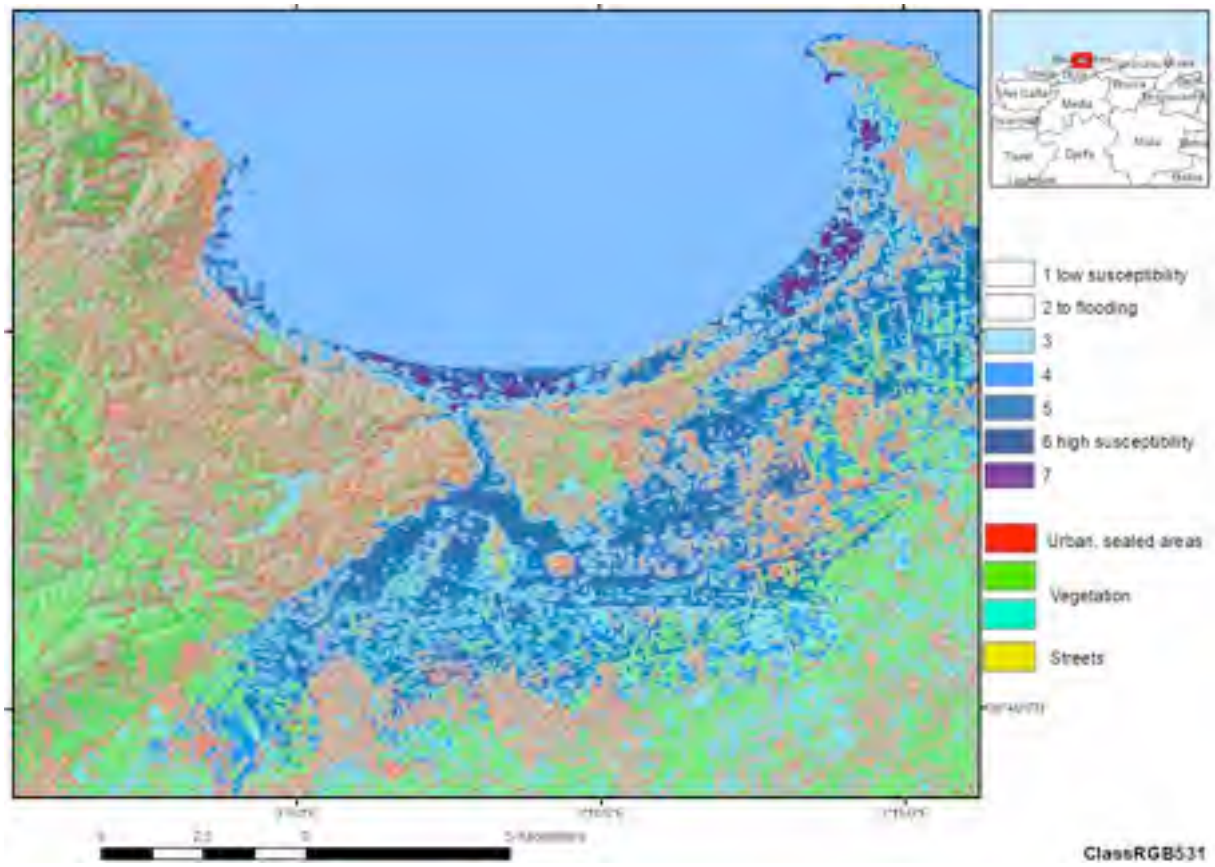

Figure 10: Results of the weighted overlay based on morphometric, causal factors in the area of Algiers

4. DISCUSSION

The purpose of this work was to test a worst-case scenario for an offshore seismogenic structure in the central part of North Algeria. The Khayr Al Din Bank and its related reverse fault system is a serious threat for seismic and tsunami hazard and risk in the coast of Algeria. Seismic shaking maps were computed and tsunami waves were simulated for a 7.5 earthquake off Algiers (Epicenter: 2.98E, 36.98N). The OpenSHA application was used to calculate the peak ground accelerations (PGA) and the peak ground velocities (PGV). The results obtained show the Algiers Massif is the most exposed region as for the seismic risk. The tsunami waves triggered from the 7.56 magnitude off Algiers reach about 1.9 meters in height in the eastern part of the Bou Ismail bay.

Areas exposed to flooding in the coastal zones of Northern-Algeria detected from remote sensing and GIS were also here present. From LANDSAT imageries and weighting tools in the GIS application, a susceptibility to flooding map was constructed / elaborated based on causal, morphometric and triggering factors for the Algiers bay. The highest susceptibility flooding levels are located in the central and eastern part of the Algiers bay.

Assessing a coastal risk from combining the Shindo Scale for earthquakes and the Papadopoulos-Imamura Scale for the tsunamis help to associate physical measurements and data (PGA, water height and flood extent) with observed impact such as (1) the damage on the infrastructure and buildings relatively to the materials used for the constructions (wooden houses, concrete, reinforced concrete, masonry, etc.) and (2) the potential effect on lifeline (Epstein, 2011; Amir et al. 2013). Both scales were used to define a new tsunami risk scale based on a tsunamigenic earthquake vulnerability index (Amir et al., 2013). The results here obtained could be used to assess a rank considering the PGA values and the tsunami velocities for the Bou Ismail bay and the Algiers bay. For that purpose, this study must be completed by additional parameters such as the liquefaction and the rockslide potential, the structural class vulnerability and the available space to evacuate for several points of interest along both bays.

5. CONCLUSION

Coastal cities and exposed communities face various sources of hazards that can impact their livelihoods. In this paper, an interdisciplinary approach was presented to discuss on the coastal risk in the Algiers region known to be a seismogenic zone. Northern Algeria is subjected to tsunami hazard and the Khair Al Din Bank and its related reverse fault are candidates for a worst-case scenario for the Algiers region. A tsunami modeling was then computed using the GeoClaw package for a 7.6 earthquake off Algiers. The surface heights and the flow velocities estimated for several points of interest near and in the coast highlight the threat coastal harbors and cities will face as for structural damage and flooding. Seismic hazard maps were as well generated using the Opensha application for ground motion modeling. The peak ground accelerations and the peak ground velocities data computed for a 7.5 earthquake off Algiers in the Khair Al Din Structure show the Algiers massif is the most exposed to structural damage. Finally, remote sensing is widely used for risk assessment and can be applied to identify locations prone to damage. The water current dynamics and the coastal morphology revealed by satellite imageries were examined

and considered to produce a GIS – map showing areas susceptible to flooding in the Algiers bay. At length, the combination of these three methods converges to same results and conclusions as for areas at risk either due to the earthquake event or the induced tsunami and its related flooding hazard.

REFERENCES

Abrahamson, N. A., & Silva, W. J. (1997). Empirical response spectral attenuation relations for shallow crustal earthquakes. *Seismological Research Letters, 68*(1), 94-127.

Amante, C., & Eakins, B. (2009). *ETOPO 1 Arc-Minute Global Relief Model : Procedures, Data Sources and Analysis* . NOAA Technical Memorandum NESDIS NDGC-24.

Amir, L. A., Cisternas, A., Dudley, W., McAdoo, B. G., & Pararas-Carayanis, G. (2013). A new tsunami risk scale for warning systems - Application to the bay of Algiers (Algeria, Western Mediterranean). *Science of Tsunami Hazards, 32*(2), 116-121.

Amir, L., Cisternas, A., Dudley, W., McAdoo, B. G., & Pararas-Carayannis, G. (2013). A new tsunami risk scale for warning systems - Application to the bay of Algiers (Algeria, West Mediterranean). *Science of Tsunami Hazards, 32*(2), 116-131.

Domzig, A., Yelles, K., Le Roy, C., Deverchere, J., Bouillin, J.-P., Bracene, R., . . . Pauc, H. (2006). Searching for the Africa-Eurasia Miocene boundary offshore western Algeria (MARADJA'03 cruise). *Comptes Rendus Geosciences, 338*(1-2), 80-91.

Epstein, W. (2011). *A Probabilistic Risk Assessment Practioner looks at the Great East Japan Earthquake and Tsunami.* Tokyo: Tokyo Institute of Technology, Ninokata Laboratory.

Field, E. H., EERI, M., Seligson, H. H., Gupta, N., Gupta, V., Jordan, T. H., & Campbell, K. W. (2005). Loss Estimates for a Puente Hills Blind-Thrust Earthquake in Los Angeles, California. *Earthquake Spectra, 21*(2), 329-338.

Field, E. H., Gupta, V., Gupta, N., Maechling, P., & Jordan, T. H. (2005). Hazard Map Calculations Using Grid Computing. *Seismological Research Letters, 76*(5), 565-573.

Field, E. H., Jordan, T. H., & Cornell, C. A. (2003). OpenSHA: A developing community-modeling environment for seismic hazard analysis. *Seismological Research Letters, 74*, 406-4019.

George, D. L., & Leveque, R. J. (2006). Finite Volume Methods and Adaptative Refinement For Global Tsunami Propagation and Local Inundation. *Science of Tsunami Hazards, 24*(5), 326-328.

Heddar, A., Authemayou, C., Djellit, H., Yelles, A., Deverchere, J., Gharbi, S., . . . Van Vliet Lanoe, B. (2012). Preliminary results of a paleoseismological analysis along the Sahel fault (Algeria): New evidence for historical seismic events. *Quaternary International*, 1-14.

Maouche, S., Morhange, C., & Meghraoui, M. (2009). Large boulder accumulation on the Algerian coast evidence tsunami events in the western Mediterranean. *Marine Geology, 262*, 96-104.

Nandasena, N., & Tanaka, N. (2013). *Boulder transport by high-energy (tsunamis): Model development for threshold entrainment and transport.* Research Report, Department of Civil and Environmental Engineering, Saitama Univ.

Okada, Y. (1992). Internal Deformation due to Shear and Tensile Faults in a Half-Space. *Bull. Seism. Soc. Am.*, 82, 1018-1040.

Theilen-Willige, B. (2014). Flooding Hazard in Northern Algeria : Contribution of remote sensing and GIS methods to the detection of areas exposed to flooding in the coastal zones of Northern Algeria. *ICT-DM 2014*, (pp. 1-4). Algiers, Algeria.

Yelles, A., Domzig, A., Deverchere, J., Bracene, R., Mercier de Lepinay, B., Strzerynski, P., . . . Djellit, H. (2009). Plio-Quaternary reactivation of the Neogene margin off NW Algiers, Algeria : The Khayr al Din bank. *Tectonophysics, 475*, 98-116.

Yelles-Chaouche, A. (1991). Coastal Algerian Earthquakes : a potential risk of tsunamis in western Mediterranean ? Preliminary investigation. *Science of Tsunami Hazards, 9*, 47-54.

Yielding, G. (1985). Control of rupture by fault geometry during the 1980 El Asnam (Algeria) earthquake. *Geophys. J. R. astr. Soc., 81*, 641-670.

ISSN 8755-6839

SCIENCE OF TSUNAMI HAZARDS

Journal of Tsunami Society International

Volume 34 Number 3 2015

VALIDATION OF JOKO TINGKIR SOFTWARE USING TSUNAMI IMPORTANCE

Madlazim[1], Tjipto Prastowo[1] and Thomas Hardy[2]

[1]Physics Department, State University of Surabaya (Unesa), Surabaya 60231
[2]Indonesian Agency for Geophysics, Climatology and Meteorology, Jakarta 10720
email: madlazim@fmipa.unesa.ac.id

ABSTRACT

Joko Tingkir program, an application for tsunami early warning, has been utilised using real-time data processing at the Research and Development Centre, Indonesian Agency for Geophysics, Climatology and Meteorology since 2013. The program can also be used to analyse earthquake events before 2013. The aim of this study is thus to validate Joko Tingkir program for an improved performance of the Indonesian tsunami early warning system using the data recorded by at least 6 seismic stations managed by BMKG-Net where data collecting for each event is limited to only 3 minutes after origin time. The data were used to determine new tsunami parameters: the duration of rupture (T_{dur}), the 50 second exceed duration (T_{50Ex}), and the dominant period (T_d). Hierarchical Product Platform Realisation Method (HPPRM), which had three different phases: defining phase, modeling phase and solving phase, was used to validate the program. This study exercises records before 2014 and during 2014-2015 available at the intranet 172.19.0.13/litbang/www. For earthquakes that occurred before 2008, we make use of IRIS DMC seismic stations at http://ww.iris.edu since BMKG-Net has not yet operated. All of the data in the present study were events having magnitudes of greater than 6.5. After a conversion of quantitative data into qualitative data, the results are compared to those of tsunami importance provided by NOAA database. It was found that there is no significant differences between the results derived from the current study and the NOAA database, leading to a conclusion that the software developed is valid.

Keywords: *Joko Tingkir software, tsunami early warning, HPPRM, tsunami importance*

Vol. 34, No. 3, page 189 (2015)

1. INTRODUCTION

After a catastrophic disaster of the Indian Ocean tsunami in December 26, 2004, several countries nearby the Ocean have all committed to the development of a tsunami early warning system. In the light of this, Indonesia has developed the Indonesian Tsunami Early Warning System (Ina-TEWS) since 2008, which automatically processes the hypocentre (epicentre and depth) and magnitude of an earthquake once it occurs. If an earthquake occurs in the oceans at a depth of < 100 km and has a magnitude of > 7, the Ina-TEWS releases a tsunami early warning, suggesting that the earthquake may then generate tsunami. However, such suggestion needs to be evaluated in some cases owing to the need for rapid information of high accuracy (Madlazim, 2011). For example, false assessment of tsunami hazard alert by the Ina-TEWS was issued for 30 events during 2007-2010, where only 8 cases were correctly announced (personal communication with BMKG authority). This indicates that the study regarding improvement of Ina-TEWS performance remains challenging and important for some reasons.

The need for a rapid, correct analysis for a particular earthquake event therefore calls for validation of a method applied in use. Pedersen *et al*. (2000) asserted that validation of a research method is a vital process for developing confidence in its usefulness with respect to a specific purpose. They associate usefulness, effectiveness and efficiency of a method with whether the method provides correctly designed solutions with acceptable performance. It follows that the solutions are desired solutions with more accurate, faster, less cost and time. Hence, the validating process aims to evaluate the effectiveness and efficiency of the method based on separate qualitative and quantitative data sets or a combined set of both.

In line with the above ideas, product validation is an important step for developing theoretical and practical aspects (Daniel *et al*., 2006). They further stated that, for example, engineers who design specific products or processes usually exercise some design methods. The methods are expected to have positive impacts of all aspects of success, including performance quality, time and cost upon users. Thus, it is reasonable to seek validation procedures for design methods similar to the ones successfully applied in medical treatment, as carried out by Daniel *et al*. (2006). In other fields, such as geophysics, the associated procedures must be well-documented, objective and evidence-based.

The Faculty of Mathematics and Natural Sciences in the State University of Surabaya (Unesa) has collaborated with the Research and Development Centre (Puslitbang) of Indonesian Agency for Geophysics, Climatology and Meteorology (BMKG) to conduct research on an enhanced reliable method for better prediction of tsunami alert in areas potential to tsunami threats since 2012. The collaboration research has been performed by implementing Joko Tingkir software and combining Graphical User Interface (GUI) from Puslitbang BMKG. The enhanced method was applied for evaluating tsunami early warning using the data collected from distributed stations accessed by BMKG-Net during the first three-minute time after origin time of the likely tsunamigenic earthquake event. As reported by Masturyono *et al*. (2013), this method was well-validated using earthquake data in 2013 with magnitudes ranging from 5.0 to 7.2 and found that the software was in good agreement with the majority (96.5%) of cases considered.

To go further, the present study has made use of field records from various places in Indonesia before 2014 and during 2014-2015 with a magnitude of > 6.5 for better accuracy, relatively

compared to previous work of Masturyono *et al*. (2013). In the process, we have adopted here a simple formula used by Lomax and Michelini (2011) to define an approximate measure of the so-called tsunami importance (I_t) for earthquake events under consideration based on a maximum water height h and 0-4 descriptive indices i of tsunami effects, such as deaths, injuries, damages, and houses destroyed given by the NOAA historical tsunami database at http://www.ngdc.noaa.gov/hazard/tsu_db.shtml, where I_t is defined as $I_t = i_{height} + i_{death} + i_{injury} + i_{damage} + i_{houses\ destroyed}$ with $i_{height} = 4, 3, 2, 1, 0$ corresponding to values for $h = 10, 3, 0.5$ m, $h > 0$, $h = 0$, respectively.

According to Lomax and Michelini (2009) and Madlazim (2013), an earthquake is said to be potential to trigger a tsunami if $I_t \geq 2$. We set $I_t = 0$ for events not listed in the database and note that I_t is approximate and unstable since it depends strongly on the instrumentation, coastal bathymetry and population density in the region, where the tsunamigenic earthquake takes place. A value of $I_t \geq 2$ directly corresponds to the Japan Meteorological Agency (JMA) threshold issued for tsunami warnings while the most devastating tsunamis typically refer to $I_t \geq 10$ (Lomax and Michelini, 2009).

The purpose of the current study is to evaluate and hence validate Joko Tingkir software as an 'additional tool' to the existing system for an improved tsunami early warning using tsunami importance. The software monitors and records real-time data, off-line *P*-wave rupture duration (T_{dur}), dominant period (T_d), and rupture duration longer than 50 s (T_{50Ex}) for large earthquakes in Indonesia with magnitudes > 6.5, observed as the vertical component of waveforms by seismometer. The validating proces is thus aimed to test whether the software developed is valid for use.

2. METHODS

As previously outlined, the methods used in this research are separated into two parts. The first method, the so-called Hierarchical Product Platform Realisation Method (HPPRM), suggested by Pedersen *et al*. (2000), having three independent different phases, that is, defining phase, modeling phase and solving phase. This method directly corresponds to validating processes of the Joko Tingkir software in use. Summarised processes in each phase are as follows. In the first phase, data were collected and processed; then in the second phase, the processed data were compared to a reference value provided by NOAA tsunami database; in the final step, well-suited problems were solved using correct decision making.

Here we provide a more detailed process in each phase. The first phase served as 'numerical taxonomy' where inputs were associated with the data collected within framework of standarised procedures by means of data gathering and/or data clustering. This step refers to an objective selection whereas data interpreting is more based on subjective judgements. The second phase, also known as 'technology diffusion', was named after considering alternative techniques according to their benefits to the existing technology. The use of discounting factor to leave factors irrelevant to the problem in this phase is objective while decisions regarding learning rates and leverage potentials are based on subjective judgements. The third phase is more about to compromise a 'decision support problem', which was used to enable model designers to achieve

their goals effectively and efficiently with respect to better operational performance, lesser operational time and operational cost. In this final phase, compromised solutions regarding the problem in question are considered objective whereas decisions based on scenarios are regarded as subjective ones.

Thus, the HPPRM is a method of validation containing logic and systematic procedures that are merely based on determination of whether the associated procedure in each step of validation processes is objective. In its performance, the validation method here is not meant to replace the existing tsunami early warning system, *i.e.*, the Ina-TEWS with a new warning system. Instead, the alternative system developed by implementing Joko Tingkir software can better influence on the Ina-TEWS, leading to an improved performance of the new tsunami early warning system.

The second method in this research directly corresponds to ways of determining enhanced tsunami prediction using Joko Tingkir software. Madlazim and Hariyono (2014) developed Joko Tingkir application to examine parameters relevant to or being indicators of an oceanic earthquake generating a tsunami. The parameters are the rupture duration (T_{dur}) and the dominant period (T_d), associated with the 'length' and 'width' of rupture zone, respectively, the exceed duration (T_{50Ex}), and the corresponding products of the three, that is, $T_{dur} \times T_d$ and $T_{50Ex} \times T_d$. Note that T_{50Ex} is referred to here as a better estimate of the 'length' of rupture zone than T_{dur}. Lomax and Michelini (2011) stated that $T_{dur} \times T_d$ and $T_{50Ex} \times T_d$ can be associated with the 'cross-sectional areas' of the rupture zone, which is proportional to the strength of the earthquake source.

The followings are flowchart of the software for calculations of new tsunami parameters: (1) readings of vertical component of *P*-wave velocity (as it gives a smaller noise relatively compared to other velocity components); (2) *P*-wave onset picking; (3) 5-20 Hz bandpass filtering; (4) determination of T_{dur}, T_d, T_{50Ex}, $T_{dur} \times T_d$ and $T_{50Ex} \times T_d$; (5) tsunami criteria testing. Design implementation of the software in relation to Ina-TEWS is shown in Figure 1.

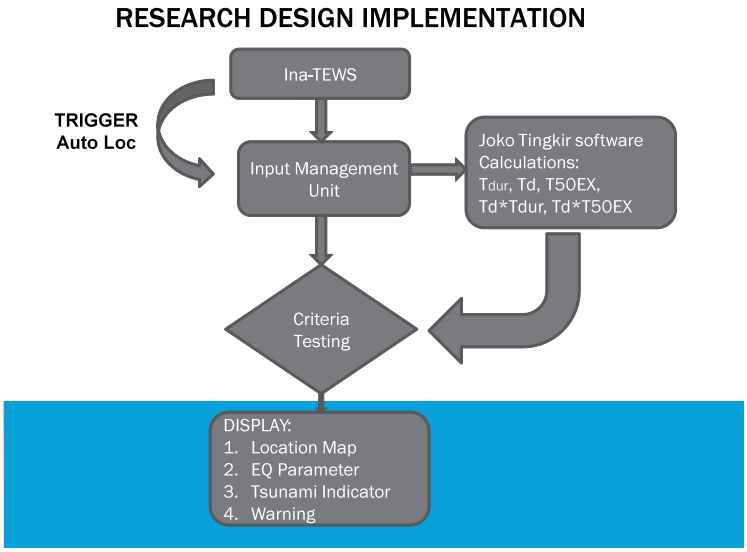

Figure 1. Design implementation of Joko Tingkir software (taken from Masturyono *et al*., 2013).

3. DATA

The data in this study were obtained from records comprising 32 events before 2014 and in 2014-2015 around the country and were provided by the intranet 172.19.0.13/litbang/www for real-time data processing. These events were monitored by grouped seismic stations that are managed by BMKG-Net covering large areas of the Indonesian archipelago, as shown in Figure 2. In addition, we also accessed IRIS DMC seismic stations at http://ww.iris.edu to further analyse 10 events before 2008 for off-line data processing, owing to the lack of real-time data at times when BMKG-Net has not yet existed in the country. All the events taken as the data have magnitudes of greater than 6.5 as these events are likely to generate tsunamis.

Figure 2. Seismic stations across large areas in Indonesia run by several countries and managed by BMKG-Net (taken from https://inatews.bmkg.go.id/new/meta_eq.php with permission from the Puslitbang BMKG authority for use of this study).

Along with the existing system, the data provided by the new tsunami warning system consist of geographical location where the event occurs, date and corresponding origin time, epicenter, depth of the earthquake source, map of the epicenter, magnitude of the earthquake, and relatively new tsunami parameters known as five discriminants: rupture duration T_{dur}, dominant period T_d, exceed duration T_{50Ex}, $T_{dur} \times T_d$ and $T_{50Ex} \times T_d$. After rapid assessment, these give directly a set of both observed and threshold values of the new tsunami parameters, from which status is given and therefore a corresponding decision for tsunami hazard alert is or is not officially declared. We here provide one case study for an example seen in Figure 3, describing how the tsunami application works.

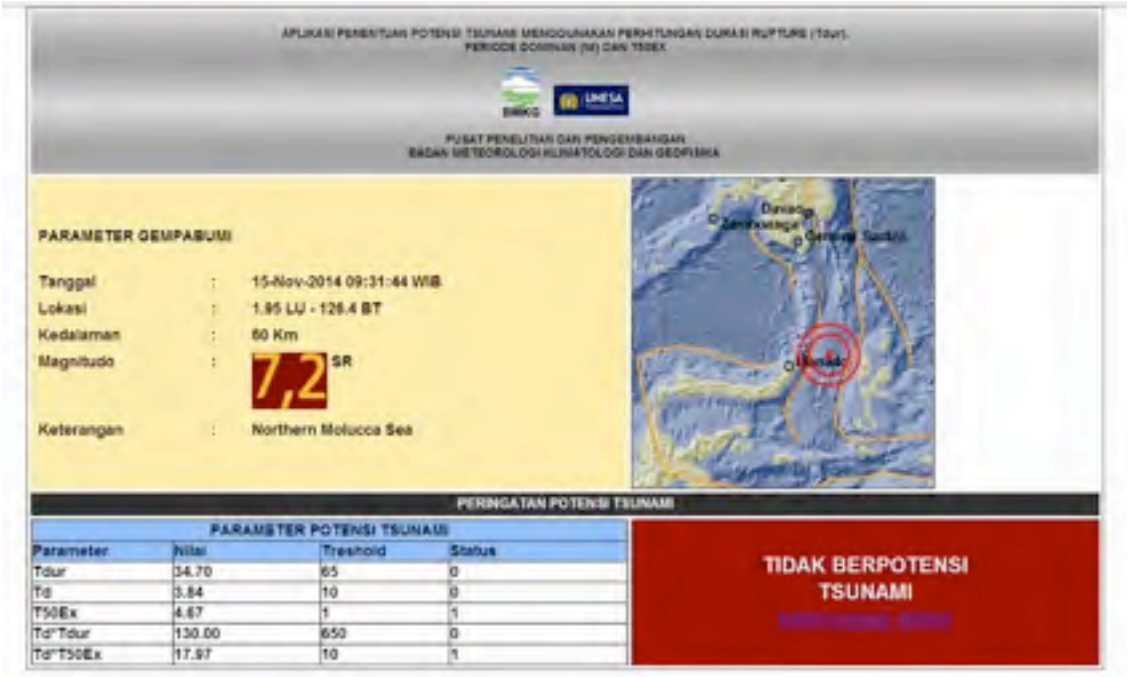

Figure 3. Performance of Joko Tingkir application as a new tsunami early warning system (Puslitbang BMKG, 2015). For a particular event, three of five discriminants having values less than corresponding thresholds, indicating that the earthquake was not a tsunamigenic event (taken from the intranet 172.19.0.13/litbang/www with permission from the Puslitbang BMKG authority for use of this study).

4. RESULTS AND DISCUSSION

Following Madlazim (2011; 2013), rapid determination of tsunami assessment using five discriminant parameters was performed using Joko Tingkir software. A set of tsunami criteria were thus as follows: $T_{dur} \geq 65$ s, $T_d \geq 10$ s, $T_{50Ex} \geq 1$ s, $T_{dur} \times T_d \geq 650$ s^2 and $T_{50Ex} \times T_d \geq 10$ s^2. When at least three parameters of the five discriminants were equal to or greater than relevant critical values or thresholds for tsunami to occur, the application would provide important complementary information for early assessment of earthquake tsunami potential. This is very important for hazard mitigation to minimise disaster risks due to the lack of reliable, rapid and accurate analyses.

As the dominant period T_d can be quickly obtained for less than a minute after the first arrival of consecutive *P*-waves, it was still possible to examine T_{dur} rapidly for an earthquake. Following the procedures of Lomax and Michelini (2009), we determined T_{dur} for an event, which was likely to exceed 50-55 s derived from a high frequency analysis of vertical component of the velocity provided by broadband seismograms. On the 5-20 Hz bandpass filtered for a set of regional seismograms, we calculated the ratio of the root-mean-square amplitudes for 50 - 60 s after the *P*-wave arrival to the root-mean-square amplitudes for the first 25 s after the *P*-wave arrival to obtain a station duration exceed level for 50-55 s. Based on these facts and previous work (Madlazim, 2011; 2013) with large earthquake data sets, we estimated that field observations from 6-15 seismic stations were needed to obtain reliable, stable valus for T_{dur}, T_{50Ex} and T_d.

Table 1 below describes the numerical results of real-time data processing for 32 events before 2014 and in 2014-2015 (available from BMKG-Net database) and the results of off-line data assessing for 10 events before 2008 (using IRIS DMC seismic stations) considered. As earlier mentioned, the data collecting was limited by the Joko Tingkir during the first three-minutes, after which an additional time of at least one minute was required for data analysing. Thus, the availability of the five period-duration tsunami discriminants (shown in the second column in Table 1) is at 4 minutes after origin time (OT). This method of rapid data assessment is approximately a minute quicker than that of using earthquake magnitudes. According to Madlazim (2011; 2013), from the five tsunami discriminants listed here: T_{dur}, T_d, T_{50Ex}, $T_{50Ex} \times T_d$ and $T_{dur} \times T_d$, three of these discriminants along with $T_{50Ex} \times T_d$ taken as the tsunami parameter discussed in Lomax and Michelini (2011) to better accurate prediction of tsunami alert than $T_{dur} \times T_d$ as the parameter used by Lomax and Michelini (2009) were observed to correctly identify 92%, 92% and 77% of the likely tsunamigenic earthquakes with $I_t \geq 2$, respectively, as tsunamis.

Table 1. Validation of the new tsunami early warning system for real-time and off-line data processing using tsunami importance (I_t).

Discriminant	Available after OT (minutes)	Critical value	Correctly identified[a]			Missed $I_t \geq 2$	False $I_t < 2$
			$I_t \geq 2$	Per cent[b]	$I_t < 2$		
magnitude	5+	M ≥ 7	9	69	19	0	14
three of five period-duration discriminants (Madlazim, 2011, 2013)	4	$T_{dur} \geq 65$ s $T_d \geq 10$ s $T_{50Ex} \geq 1$ s $T_{50Ex}\ T_d \geq 10$ s^2 $T_{dur}\ T_d \geq 650$ s^2	12	92	28	0	2
$T_{50Ex}\ T_d$ (LM-11)	4	10	12	92	28	0	2
$T_{dur}\ T_d$ (LM-09)	4	650	10	77	26	3	3

Note: [a] 13 of 42 events classified tsunamigenic; [b] the percentage of correctly identified events with $I_t \geq 2$. LM-09 refers to Lomax and Michelini (2009); LM-11 refers to Lomax and Michelini (2011).

Table 1 also describes missed cases and false warnings for all the data used in this study, consecutively given in the last two columns. Missed cases were those in the assessment that cannot be processed due to many noises disturbed. False warnings could be adequately large earthquakes with magnitudes of greater than 6.5 and were issued as tsunamis but they in fact did not exist or events having relatively small magnitudes and thus were not declared as danger but generating tsunamis.

Using three of the five tsunami parameters, no missed cases with $I_t \geq 2$ were reported by Madlazim (2011; 2013), as well as using the product of $T_{50Ex} \times T_d$ for the same cases found by Lomax and Michelini (2011), including an oceanic strike-slip earthquake with $I_t = 6$ and $M_w = 7.5$ of the Sulawesi May 4, 2000 event (shown in the first row in Table 1). In contrast, three cases

were observed by Lomax and Michelini (2009) but with only a 77% reliability of identification (shown in the last row in Table 1).

A total of 21 (14+2+2+3) cases in the last column were announced as false warnings or tsunamigenic events, where most of these cases have $I_t = 1$ and hence producing only small tsunamis. The large uncertainty in a 14 false-warning case using earthquake magnitudes as a discriminant indicates that this method is unreliable to predict whether a tsunami is generated. This is also supported by the percentage (less than 70%) of all events correctly issued for tsunamis using the magnitude method. For all the data, a total of 13 earthquakes (containing 13 of 32 cases before 2014 and in 2014-2015 and a zero record of 10 events before 2008) were then classified as tsunamigenic events as they go with $I_t \geq 2$. The detailed results of numerical calculation of the parameters are given below.

As demonstrated in Table 1, calculations of tsunamigenic-potential earthquakes based on the new five discriminants do not require accurate knowledge of either earthquake location or magnitude for most of all events. The overall performance of the discriminants is marginally better than that of the magnitude parameter having 69% of cases correctly identified, where field data with magnitudes of equal to or greater than 7 for the magnitude discriminant were used by the Ina-TEWS (but with no Joko Tingkir software inserted into the existing system).

The results also capture another feature of the nature of calculations using the new tsunami parameters. The period-duration discriminants gave mixed results to identify tsunami potential of oceanic, inter-plate thrust and strike-slip events. Some of these events may be falsely identified as tsunamigenic (when they are high magnitudes or long rupture durations) since tsunami excitation for vertical, strike-slip faults is very low, relatively compared to other faulting types (*e.g.*, Kajiura, 1981). In contrast, other oceanic, inter-plate thrust and strike-slip events may be missed as tsunamigenic (*i.e.*, when they have moderate magnitudes or rupture durations) because tsunami excitation in these cases can be augmented by the horizontal displacement of ocean floor topography (Tanioka and Satake 1996), an effect somewhat independent of the source size, measured as length, width, and displacement (*LWD*) and thus is not well-quantified by any of all the discriminants. The results for all cases presented in this study demonstrate that with a large certainty in the numerical calculations (more than ninety per cents of reliability in calculation) three of the new five discriminants together with a $T_{50Ex} \times T_d$ parameter can identify tsunami generation at seas better than both $T_{dur} \times T_d$ and T_{dur} parameters. A plausible reason of this fact is that determination of T_{dur} is not adequately accurate for local events (Lomax and Michelini, 2009).

5. CONCLUSIONS

Joko Tingkir software as a new tool for a rapid analysis of tsunami hazard assessment has been implemented using real-time and off-line data flow within the Ina-TEWS Network for validation purposes. The validating process shows that 92 % of total 42 events comprising 32 events (before 2014 and during 2014-2015) and 10 events (before 2008) with magnitudes greater than 6.5 tested are consistent with a set of tsunamigenic criteria derived for HPPRM validation method. The criteria are $T_{dur} \geq 65$ s, $T_d \geq 10$ s, $T_{50Ex} \geq 1$ s, $T_{dur} \times T_d \geq 650$ s^2 and $T_{50Ex} \times T_d \geq 10$ s^2 for oceanic earthquakes generating tsunamis. Relatively compared to tsunami importance I_t, no

significant differences are found between the current results derived from the software and those obtained from the NOAA database. These findings bring into a simple conclusion that the Joko Tingkir is firmly valid for use.

The total time required for all assessment processes begining from data collection up to data processess takes about 4 minutes, directly measured from the origin time of a particular earthquake. This is made possible by the Trigger – an effective instructional syntax used in the program – that analyses system automatic location to work on determining the depth and epicentre, or equally like, the hypocentre, of the eartquake source and at the same time calculating all the new five tsunami discriminants. Therefore, the method of validation and the method of rapid, accurate assessment of tsunami hazard proposed in the present study are valid and worth to put into effect in the fields.

ACKNOWLEDGEMENTS

We thank the Puslitbang BMKG and IRIS DMC (http://ww.iris.edu) for providing data access used and people who help supporting facilities needed in this study. Sincerely thanks go to Anthony Lomax and Alberto Michelini for fruitful discussions and useful guidance in estimating rupture duration, dominant period and T_{50Ex} for Joko Tingkir software parameters, and to George Pararas-Carayannis for his best to edit some parts of the manuscript for clarity. The work was also supported by the DP2M, Directorate General of Higher Education, Ministry of National Education and Culture, Republic of Indonesia for the award of research fund under entitled National Strategic Research Grant No. 053.11/UN38.11P/LT/2015 dated March, 5 2015.

REFERENCES

Daniel D., Frey, Clive L., Dym, 2006. Validation of design methods: lessons from medicine. *Research in Engineering Design*, **17**: 45-57, doi: 10.1007/s00163-006-0016-4.

Kajiura, K., 1981. Tsunami energy in relation to parameters of the earthquake fault model. *Bull. Earthq. Res. Inst.,* **56,** 415–440.

Lomax, A. and Michelini, A., 2009. Tsunami early warning using earthquake rupture duration. *Geophys. Res. Lett*., **36**, L09306, doi:10.1029/2009GL037223.

Lomax, A. and Michelini, A., 2011. Tsunami early warning using earthquake rupture duration and *P*-wave dominant period: the importance of length and depth of faulting. *Geophys. J. Int*., **185**, 283-291, doi: 10.1111/j.1365-246X.2010.04916.x.

Madlazim, 2011. Towards Indonesian tsunami early warning system by using rapid rupture duration calculation. *Science of Tsunami Hazards*, **30**(4).

Madlazim, 2013. Assessment of tsunami generation potential through rapid analysis of seismic parameters - case study: comparison of the earthquakes of 6 April and of 25 October 2010 of Sumatra. *Science of Tsunami Hazards*, **32**(1).

Madlazim and Hariyono, E., 2014. Joko Tingkir program for estimating tsunami potential rapidly. *AIP Conf. Proc*., 1617, **57**, http://dx.doi.org/10.1063/1.4897103.

Masturyono, Hardy, T., Madlazim and Karyono, 2013. Validation of Joko Tingkir software in the real-time tsunami warning system: a preliminary result. the 3rd International Symposium on Earthquake and Disaster Mitigation (ISEDM), Yogyakarta, 17-18 December 2013.

Pedersen K., Emblemsvåg, J., Bailey, R., Janet K. Allen and Mistree, F., 2000. Validating design methods and research: the validation square. *DETC Proceedings*, '00 2000 ASME, September 10-14, 2000, Baltimore, Maryland.

Tanioka, Y. and Satake, K., 1996. Tsunami generation by horizontal displacement of ocean bottom. *Geophys. Res. Lett.,* **23**(8), 861–864.

ISSN 8755-6839

SCIENCE OF **TSUNAMI HAZARDS**

Journal of Tsunami Society International

Volume 34 **Number 3** **2015**

TSUNAMI SOCIETY INTERNATIONAL, 1741 Ala Moana Blvd. #70, Honolulu, HI 96815, USA.

WWW.TSUNAMISOCIETY.ORG